# 20 Ionic Transport in Disordered Materials

Armin Bunde, Wolfgang Dieterich, Philipp Maass, and Martin Meyer

## 20.1 Introduction

The low-frequency dynamic response of many non-metallic materials is governed by the transport of mobile ions or other charged mobile defects. The classes of such materials include traditional ionic glasses, polymeric and glassy superionic conductors, highly defective crystals or even highly viscous liquids such as glassforming melts. To get an understanding of the microscopic transport mechanism in these materials, a large number of experimental techniques has been applied, among them are tracer experiments (Chap. 1 and [1]), conductivity measurements including impedance spectroscopy (Chap. 21, [2–5]), nuclear magnetic resonance (NMR) relaxation (Chap. 9, [6–10]), quasielastic neutron scattering (Chaps. 2, 3 and 13, [11, 12]), internal friction and ultrasonic absorption measurements (Brillouin scattering) (Chap. 11, [13, 14]). In all these experiments the measured quantities show characteristic deviations from the standard behavior that one would expect for a purely random motion of the mobile ions.

For example, the dynamic conductivity $\hat{\sigma}(\omega)$ in disordered crystalline and glassy ionic conductors exhibits, for fixed temperature $T$, a dc-plateau at low frequencies (below some crossover frequency $1/\tau_\sigma$), and follows an approximate power law behavior at larger frequencies [15],

$$\hat{\sigma}(\omega) \sim \begin{cases} \sigma_{\text{dc}}, & \omega\tau_\sigma \ll 1, \\ (i\omega)^{n_\sigma}, & \omega\tau_\sigma \gg 1. \end{cases} \tag{20.1}$$

The dc conductivity $\sigma_{\text{dc}}$ usually shows an Arrhenius behavior below the glass transition temperature,

$$\sigma_{\text{dc}}T = A_\sigma \exp(-E_\sigma/k_{\text{B}}T), \tag{20.2}$$

and also the crossover frequency $\tau_\sigma^{-1}$ is thermally activated with the same activation energy $E_\sigma$. The exponent $n_\sigma > 0$ tends to increase, if the temperature is lowered or if the frequency is increased by several orders of magnitude. From standard random walk theory on a lattice with equivalent sites one would expect no dispersion to occur, i.e. $n_\sigma = 0$ (see Sect. 20.2.2). The overall behaviour (20.1) is not restricted to ionically conducting solids but

occurs also in disordered electronic conductors such as amorphous semiconductors, electronic conducting polymers and disordered polaronic conductors. The widespread occurrence of such similar low-frequency dielectric behavior in all disordered solids was first pointed out by Jonscher [16] and is known as the "universal dielectric response".

A second, "universal" type of response in disordered ionic systems occurs at even higher frequencies, $\omega > \omega_{\mathrm{NCL}} \gg \tau_\sigma^{-1}$. Going at ambient temperatures to the Gigahertz regime, the real part of the conductivity increases nearly linearly with frequency,

$$\mathrm{Re}\,\hat{\sigma}(\omega) \sim \omega; \quad \omega > \omega_{\mathrm{NCL}}. \tag{20.3}$$

This is equivalent with a frequency-independent dielectric loss, $\chi''(\omega) \simeq$ const, and is thus known as "nearly constant loss" (NCL) response [17–19]. Its temperature dependence is much weaker than implied by (20.2) and (20.1) with the consequence that at low temperatures the NCL response dominates the spectrum in the experimentally accessible frequency-range.

In some glassy fast ion conductors it was found that the dc-conductivity shows strong deviations from a simple Arrhenius law even below the glass transition temperature [20, 21]: The values of $\sigma_{\mathrm{dc}}$ at ambient temperatures are significantly smaller than expected when extrapolating the Arrhenius law valid at low temperatures $T$. We note that a non-Arrhenius behaviour was found earlier in ion conducting glasses but disappeared after annealing [22].

Strongly non-Arrhenius diffusion of a different type occurs in yet another class of amorphous materials, namely ion conducting polymers above their glass transition temperature [23]. Certain chain polymers carry polar groups in their repeat unit and are therefore capable of dissolving salts. When temperature is lowered, the polymer chains tend to freeze. In contrast to (20.2), the strong coupling of ions to the network degrees of freedom generally leads to Vogel-Fulcher-Tammann (VFT)-type behavior [24] of the conductivity,

$$\sigma_{\mathrm{dc}}T \propto \exp(-E/k_{\mathrm{B}}(T - T_{\mathrm{VFT}})) \tag{20.4}$$

Here $E$ is an energy parameter and $T_{\mathrm{VFT}}$ the VFT-temperature, commonly referred to as "ideal glass transition temperature". Much effort is being spent to explore transport mechanisms in these complex materials, and to optimize their electrical conduction properties with respect to their use in electrochemical devices.

Apart from conduction and dielectric measurements, the perhaps most common experimental technique to probe ionic motion in disordered media is nuclear magnetic resonance (see Chap. 9). The behavior of the diffusion-induced spin-lattice relaxation (SLR) rate $1/T_1(\omega_{\mathrm{L}}, T)$, as a function of temperature $T$ and Larmor frequency $\omega_{\mathrm{L}}$, can be summarized as follows:

$$\frac{1}{T_1}(\omega_{\mathrm{L}}, T) \sim \begin{cases} \exp(E_1^{\mathrm{SLR}}/k_{\mathrm{B}}T)\,, & T \gg T_{\max}(\omega_{\mathrm{L}}), \\ \omega_{\mathrm{L}}^{n_{\mathrm{SLR}}-2} \exp(-E_2^{\mathrm{SLR}}/k_{\mathrm{B}}T)\,, & T \ll T_{\max}(\omega_{\mathrm{L}}), \end{cases} \tag{20.5}$$

with an exponent $n_{\mathrm{SLR}} \geq 0$. In an Arrhenius plot, $1/T_1$ shows a maximum at $1/T_{\max}(\omega_{\mathrm{L}})$, where the temperature $T_{\max}(\omega_{\mathrm{L}})$ decreases with decreasing frequency. Since generally $E_1^{\mathrm{SLR}} > E_2^{\mathrm{SLR}}$, the curve is asymmetric in shape. In contrast to this overall behavior, the standard Bloembergen-Purcell-Pound (BPP) theory [25] predicts a symmetric maximum of $1/T_1$ in the Arrhenius plot with $n_{\mathrm{SLR}} = 0$ (see Sect. 20.2.4).

Dynamic scattering of neutrons is another technique to investigate the ionic transport. In many structurally disordered ionic conductors broad quasielastic components in the scattering spectra are observed. The line shapes of these components often deviate from simple Lorentzians, which are expected in the simple random walk case (see Sect. 20.2.3). A similar behavior has been found in mechanical loss spectroscopy [13, 14]. The spectra are usually much broader than simple Debye spectra, reflecting an inherent non-exponential nature of the ionic relaxation processes.

From a theoretical point of view, the ionic transport in solids is a very complex phenomenon (for a recent review, see [26]) and rigorous solutions are not available. For an ordered host lattice a mode-coupling theory has been developed to study the effect of Coulomb interactions between the mobile ions [27]. One fundamental consequence of the long-range nature of Coulomb forces is the non-analytic dependence of the tracer diffusion coefficient on the ion concentration $c$ in dilute systems, $c \to 0$. To describe the experimental situation for arbitrary $c$ and arbitrary frequencies, however, it has turned out that also the structural disorder plays an essential role [28–30]. Various phenomenological and semi-microscopic approaches have been successfully applied. Prominent examples are the coupling scheme proposed by Ngai [31], the jump relaxation model pioneered by Funke [11] that recently was extended by means of the concept of mismatch and relaxation, see Chap. 21, and the diffusion-controlled relaxation model elaborated by Elliott and Owens [32]. Attempts have been made to map the dynamics of the many body problem onto the dynamics of a single particle moving in a complex energy landscape (see Chap. 18, [33–35]).

For a more microscopic description of the ionic transport one is dependent upon numerical investigations. Important microscopic insight emerged from recent molecular dynamics studies [36–38]. In this chapter we are mainly concerned with the results of semi-microscopic Monte Carlo studies [28–30, 39–41], where the effects of long-range Coulomb interactions between the mobile ions and structural disorder in the host lattice are investigated in a systematic way. The chapter is organized as follows. In Sect. 20.2 the basic dynamic quantities under study are defined and discussed with respect to their standard behaviour, obtained from simple random walk theory. In Sects. 20.3 and 20.4 we introduce different versions of the Coulomb lattice gas model pertaining to glasses, and represent computed relaxation spectra. In Sect. 20.5 the origin of the non-Arrhenius behavior seen in fast conducting glasses is investigated. Interacting Coulombic traps are considered in Sect.

20.6 as a mechanism that can explain the NCL response. Peculiarities in the transport properties associated with compositional changes in ion conducting glasses are discussed in Sect. 20.7. In Sect. 20.8 we turn to polymer electrolytes and present calculations of their typical transport properties as a function of temperature, pressure and salt content. Sect. 20.9 finally concludes the paper with a brief summary and discussion. For ionic transport in systems with disorder on macroscopic length scales we refer to Chap. 22.

## 20.2 Basic Quantities

In this section we discuss the standard behavior of the basic quantities of interest. We assume that the mobile particles perform simple random walks on a $d$-dimensional (cubic) lattice with lattice constant $a$. The lattice has length $L$ and the particle density is $\rho = N/L^d$, where $N$ is the number of particles. We assume that the mean residence time $\tau_0$ between two jumps of a particle is $\tau_0 = \tau_\infty \exp(V_0/k_B T)$, where $\tau_\infty$ is a rattling time and $V_0$ is the structural energy barrier between two nearest neighboring lattice sites.

### 20.2.1 Tracer Diffusion

The tracer diffusion coefficient $D$ is related to the long time limit of the mean square displacement $\langle r^2(t) \rangle$ of a tracer particle, $D = \lim_{t \to \infty} \langle r^2(t) \rangle / 2dt$. Experimentally, $D$ can be obtained from the concentration profile of radioactive tracers introduced into the material under investigation (see Chap. 1).

It is convenient to define (in $d$ dimensions) a generalized frequency-dependent tracer diffusion coefficient $\hat{D}(\omega)$ by

$$\hat{D}(\omega) = -\frac{\omega^2}{2d} \lim_{\epsilon \to +0} \int_0^\infty \langle r^2(t) \rangle e^{i\omega t - \epsilon t} dt, \qquad (20.6)$$

which for $\omega \to 0$ approaches $D$.

If the particles perform simple random walks, subsequent jumps of a tracer particle are uncorrelated and the mean square displacement increases linearly with time according to $\langle r^2(t) \rangle = a^2 t / \tau_0$, yielding $\hat{D}(\omega) = D = a^2/2d\tau_0$, independent of frequency. If the particle hops are correlated, $\langle r^2(t) \rangle$ only increases linearly for very small and very large times, and one can define a tracer correlation factor $f_{tr}$ as the ratio of the long-time diffusion coefficient $D$ and the short-time diffusion coefficient $D_{st}$ by $f_{tr} \equiv D/D_{st}$. The deviation of $f_{tr}$ from unity can be regarded as a measure of the strength of the correlations. If a particle prefers to jump back to the site where it came from (backward correlations) $f_{tr} < 1$; if it prefers to jump forward (forward correlations), we have $f_{tr} > 1$.

## 20.2.2 Dynamic Conductivity

The dynamic conductivity $\hat{\sigma}(\omega)$ can be expressed by the auto-correlation function $\langle \boldsymbol{j}(t) \cdot \boldsymbol{j}(0) \rangle$ of the current density in the absence of the electric field (Kubo formula, [42]):

$$\hat{\sigma}(\omega) = \frac{L^d}{dk_{\mathrm{B}}T} \lim_{\epsilon \to +0} \int_0^\infty \langle \boldsymbol{j}(t) \cdot \boldsymbol{j}(0) \rangle \mathrm{e}^{\mathrm{i}\omega t - \epsilon t} \mathrm{d}t. \tag{20.7}$$

The brackets $\langle \rangle$ denote a thermal average and the current density is given by the sum over the particle velocities, $\boldsymbol{j}(t) = (e\rho/N) \sum_{i=1}^N \boldsymbol{v}_i(t)$, where $e$ is the charge of the particles. (For non-interacting particles the charge $e$ means only a formal coupling to the external electric field.) Separating the velocity autocorrelation function $\langle \boldsymbol{v}_i(t) \cdot \boldsymbol{v}_i(0) \rangle \equiv \langle \boldsymbol{v}(t) \cdot \boldsymbol{v}(0) \rangle$ from the cross-correlation part, we can write

$$\langle \boldsymbol{j}(t) \cdot \boldsymbol{j}(0) \rangle = \frac{\rho e^2}{L^d} \left[ \langle \boldsymbol{v}(t) \cdot \boldsymbol{v}(0) \rangle + \frac{1}{N} \sum_{i \neq j}^N \langle \boldsymbol{v}_i(t) \cdot \boldsymbol{v}_j(0) \rangle \right]. \tag{20.8}$$

In the absence of interactions between the mobile particles, the cross terms in (20.8) vanish, $\langle \boldsymbol{v}_i(t) \cdot \boldsymbol{v}_j(0) \rangle = 0$ for $i \neq j$. Using that together with (20.6), (20.7) and the relation $2\langle \boldsymbol{v}(t) \cdot \boldsymbol{v}(0) \rangle = \mathrm{d}^2 \langle r^2(t) \rangle / \mathrm{d}t^2$ one obtains the Nernst-Einstein relation for non-interacting particles,

$$\hat{\sigma}(\omega) = \frac{\rho e^2}{k_{\mathrm{B}}T} \hat{D}(\omega). \tag{20.9}$$

For the simple random walk case, this yields $\hat{\sigma}(\omega) = \rho e^2 a^2 / 2dk_{\mathrm{B}}T\tau_0$ independent of $\omega$. In interacting systems, on the other hand, cross-correlations are non-negligible. Equation (20.9) is then generalized to

$$\hat{\sigma}(\omega) = \frac{\rho e^2}{k_{\mathrm{B}}T \hat{H}_{\mathrm{R}}(\omega)} \hat{D}(\omega) \tag{20.10}$$

where $\hat{H}_{\mathrm{R}}(\omega)$ is the complex Haven ratio. For frequencies $\omega$ much larger than the hopping rate the cross-correlations vanish even if the particles interact and $\hat{H}_{\mathrm{R}}(\omega)$ approaches one. In the limit $\omega \to 0$, $\hat{H}_{\mathrm{R}}(\omega)$ approaches the ordinary Haven ratio $H_{\mathrm{R}} = \rho e^2 D / k_{\mathrm{B}}T\sigma_{\mathrm{dc}}$.

## 20.2.3 Probability Distribution and Incoherent Neutron Scattering

For a more detailed description of the diffusion process, one considers the distribution function $P(\boldsymbol{r}, t)$, also called the "propagator" (see e.g. Chaps. 10, 19 and 23), which denotes the probability for an ion to be on a (lattice) site

$r$ at time $t$, if it started at $t = 0$ from site $\mathbf{0}$. The Fourier transform of $P(\mathbf{r}, t)$ is the incoherent structure factor $S_{\mathrm{inc}}(\mathbf{k}, \omega)$ (see Chaps. 3, 13 and 23),

$$S_{\mathrm{inc}}(\mathbf{k}, \omega) = \frac{1}{2\pi} \int \mathrm{d}^3 r \int \mathrm{d}t \, P(\mathbf{r}, t) \mathrm{e}^{-\mathrm{i}(\mathbf{k}\cdot\mathbf{r} - \omega t)} \equiv \frac{1}{2\pi} \int \mathrm{d}t \, S_{\mathrm{inc}}(\mathbf{k}, t) \mathrm{e}^{\mathrm{i}\omega t}, \tag{20.11}$$

which contributes to the differential cross section obtained in scattering experiments.

For simple random walks on a Bravais lattice, the intermediate scattering function $S_{\mathrm{inc}}(\mathbf{k}, t)$ decays exponentially

$$S_{\mathrm{inc}}(\mathbf{k}, t) = \exp\left(-\Lambda(\mathbf{k}) \frac{|t|}{\tau_0}\right), \tag{20.12}$$

with $\Lambda(\mathbf{k}) = \sum_{\mathbf{d}} (1 - \cos(\mathbf{d}\,\mathbf{k}))/\nu$, where the sum runs over all nearest-neigbor vectors $\mathbf{d}$ and $\nu$ is the number of nearest neigbors. Accordingly, $S_{\mathrm{inc}}(\mathbf{k}, \omega)$ is a simple Lorentzian with width $\Lambda(\mathbf{k})/\tau_0$.

### 20.2.4 Spin-Lattice Relaxation

In an external static magnetic field $\mathbf{B}$, the alignment of the nuclear magnetic moments of the mobile ions gives rise to a total magnetization in the direction of the applied field (see Chap. 9). By a radiofrequency pulse perpendicular to the static field this magnetization can be rotated into the opposite direction. Fluctuating local magnetic and electric fields cause the magnetization to relax into the original direction parallel to the static field $\mathbf{B}$ in a characteristic time $T_1$. The spin-lattice relaxation rate $1/T_1$ depends on both the magnitude of the field $\mathbf{B}$ and the temperature $T$. In the case of ionic conductors mainly two mechanisms give rise to the fluctuating local fields:

(i) The magnetic dipole-dipole interaction between the mobile particles.

(ii) The interaction of the nuclear quadrupole moment of one particle with the electric field gradient of another particle (as far as the ions have nuclear spin larger than $1/2$ and the quadrupole moment of the nucleus does not vanish).

According to standard theory (Sects. 9.2 and 9.9 in Chap. 9, [43, 44]), $1/T_1$ is determined by the spectral densities $J^{(1)}(\omega)$ and $J^{(2)}(\omega)$ at $\omega = \omega_{\mathrm{L}}$ and $\omega = 2\omega_{\mathrm{L}}$, respectively,

$$\frac{1}{T_1} = C(J^{(1)}(\omega_{\mathrm{L}}) + J^{(2)}(2\omega_{\mathrm{L}})), \tag{20.13}$$

where $\omega_{\mathrm{L}} = \gamma B$ is the Larmor frequency. The spectral densities are the Fourier transforms of the SLR correlation functions $G^{(q)}(t)$,

$$J^{(q)}(\omega) = \int_{-\infty}^{\infty} G^{(q)}(t) \mathrm{e}^{\mathrm{i}\omega t} \, \mathrm{d}t, \quad q = 1, 2. \tag{20.14}$$

In both cases (i) and (ii) the correlation functions $G^{(q)}(t)$ can be written as [44]

$$G^{(q)}(t) = \frac{1}{N} \sum_{i \neq j}^{N} \langle F_{ij}^{(q)*}(t) F_{ij}^{(q)}(0) \rangle, \qquad (20.15)$$

where $F_{ij}^{(q)}(t) = q(8\pi/15)^{1/2} Y_2^q(\Omega_{ij}(t))/r_{ij}^3(t)$ is the local field between the particles $i$ and $j$. $Y_2^q$ are the spherical harmonics, and $\Omega_{ij}$ and $r_{ij}$ are the spherical coordinates of the vector $\boldsymbol{r}_{ij}$ pointing from particle $i$ to particle $j$, with respect to the magnetic field. The constant $C$ in (20.13) depends on the nuclear properties of the mobile particles, $C = (3/2)\gamma^4\hbar^2 I(I+1)$ in case (i) and $C = (3/2)(e^2Q/\hbar)^2 I(I+1)/(I(2I-1))^2$ in case (ii). Here $\gamma$ is the magnetogyric ratio, $I$ the spin and $Q$ the quadrupole moment of the nucleus.

The ansatz $G^{(q)}(t) = G^{(q)}(0)\mathrm{e}^{-t/\tau_0}$, commonly referred to as the BPP ansatz [25], leads to

$$\frac{1}{T_1} = CG^{(1)}(0) \left[ \frac{\tau_0}{1+(\omega_L\tau_0)^2} + \frac{4\tau_0}{1+(2\omega_L\tau_0)^2} \right] \qquad (20.16)$$

where we have used $G^{(2)}(0) = 4G^{(1)}(0)$ valid for an isotropic distribution of the ions [43]. In an Arrhenius plot of $\ln 1/T_1$ versus inverse temperature, the curve is symmetric in shape with slopes equal to $V_0$ and $-V_0$ on the high and low temperature side of the $1/T_1$ maximum, which occurs at $\omega_L\tau_0 \approx 1$. $V_0$ is the activation energy. At the low temperature side, $\omega_L\tau_0 \gg 1$, $1/T_1$ decreases as $\omega_L^{-2} = (\gamma B)^{-2}$ with increasing field $B$.

It may be shown [30] that for simple random walks the *asymptotic* decay of $G^{(q)}(t)$ is algebraic rather than exponential. However, for (20.16) to be approximately valid it is sufficient that the correlation functions decay linearly with $t$ for small times and faster than $1/t$ for large times. Since both conditions are satisfied in the simple random walk case (for $d = 3$), the deviations from the exponential decay do not lead to pronounced changes of the standard behavior of $1/T_1$, according to (20.16).

## 20.3 Ion-Conducting Glasses: Models and Numerical Technique

As discussed in the introduction (Sect 20.1), in most cases strong deviations from the standard behavior are experimentally observed. We will show below that for a more realistic description of the ionic transport that goes beyond the simple random walk case, one has to take into account at least (a) the Coulomb interaction between the mobile charge carriers and (b) the structural disorder of the host system.

In glassy systems the ions cannot enter all regions of the substrate but are confined to diffusion paths with high mobility. Starting from a lattice

gas model allowing nearest-neighbor hops, we thus make only a fraction $p$ of lattice sites accessible for the mobile ions, totally blocking the rest of them. This construction is known as the site percolation model (Chap. 22, [45]). For $p$ well above the percolation threshold $p_c$ ($p_c \cong 0.312$ for the sc lattice), most of the accessible sites belong to the "infinite percolation cluster" (IPC), which connects opposite sides of the lattice. We disregard the small finite clusters of accessible sites in the system and consider as our model for structural disorder only the IPC where all mobile ions exhibit long-range mobility (see Chap. 22 for a sketch of the IPC). This disordered structure of accessible sites is reminiscent to a "connective tissue" or a "crumbled handkerchief", which has been suggested to model diffusion paths in ionic glasses [46]. In the detailed numerical procedure we choose a simple cubic lattice of length $L$ with lattice constant $a$ and use periodic boundary conditions. A fraction $1-p$ ($p > p_c$) of the lattice sites is randomly blocked and the IPC is determined with the help of the Hoshen-Kopelmann algorithm [47].

The simple percolation model is sufficient to explain anomalous features found in the relaxation spectra. However, it cannot explain the non-Arrhenius behaviour observed in some fast ion conductors. In order to take into account the energy scale associated with the disorder present in the diffusion paths itself, we will also study a modified model, where instead of simply blocking sites for the ions, an energy $\epsilon_i$ is assigned to each lattice site $i$ drawn from a Gaussian distribution $P(\epsilon)$ with zero mean and variance $\sigma_\epsilon^2$ (see Chap. 18). The percolative disorder can be regarded as a limiting case, where only two site energies are allowed, one being zero (with probability $p$) and one being infinite (with probability $1 - p$).

In network glasses modified by alkali-oxides or -sulfides the diffusing alkali ions will experience the Coulomb fields arising from immobile counterions. At low doping level, this leads to the picture of well-separated, negatively charged Coulomb traps, fixed at random positions $\boldsymbol{R}$, which temporarily can bind the diffusing cations and thus will have a strong influence on the conduction process. To implement such a mechanism, we assume that cations diffuse on a simple cubic lattice where a fraction $c \ll 1$ of randomly selected unit cubes carry a counterion at their midpoint $\boldsymbol{R}$. The eight corner sites of each such cube will then constitute the binding sites for the mobile ions.

In the framework of Coulomb lattice gases, those three models of disorder in the site energies can be summarized as follows:

I)    Percolative disorder

$$\epsilon_i = \begin{cases} 0 & \text{probability } p \\ \infty & \text{probability } 1 - p \end{cases} \tag{20.17}$$

II)   Gaussian disorder

$$P(\epsilon) = (2\pi\sigma_\epsilon^2)^{-1/2} \exp(-\epsilon/2\sigma_\epsilon^2) \tag{20.18}$$

III) Randomly placed counterions

$$\epsilon_i = -\sum_{\boldsymbol{R}} \frac{n_{\boldsymbol{R}} e^2}{|\boldsymbol{r}_i - \boldsymbol{R}|} \quad . \tag{20.19}$$

If $c$ is the number of mobile ions per lattice site, then with probability $c$, $n_{\boldsymbol{R}} = 1$, otherwise $n_{\boldsymbol{R}} = 0$. In this way charge neutrality is maintained.

In all these models, we assume that sites cannot be occupied by more than one ion. The strength of the Coulomb interaction relative to the thermal energy $k_{\mathrm{B}}T$ is characterized by $\Gamma \equiv V_{\mathrm{c}}/(k_{\mathrm{B}}T)$, where $V_{\mathrm{c}} \equiv e^2/r_{\mathrm{s}}$ is the typical interaction energy and $r_{\mathrm{s}} \equiv (3/4\pi\rho)^{1/3}$ the half mean distance between the mobile ions. Here $\rho = c/a^3$ denotes the ionic number density.

To model the diffusion process we use a standard Monte Carlo algorithm: In each elementary step of the simulation, an ion is chosen randomly, and a nearest neighbor site is also chosen, to which the ion attempts to jump. If the neighboring site is blocked or occupied by another ion, the jump is rejected. If the neighboring site is vacant, the ion jumps to it with probability $w = \min\{1, \exp(-\Delta E/k_{\mathrm{B}}T)\}$, where $\Delta E$ is the change of the total energy caused by the jump and is given by $\Delta E = \Delta E_{\mathrm{s}} + \Delta E_{\mathrm{c}}$. Here $\Delta E_{\mathrm{s}} = \epsilon_j - \epsilon_i$ is the site energy difference ($\Delta E_{\mathrm{s}} \equiv 0$ for the percolation model) and $\Delta E_{\mathrm{c}}$ is the energy difference due to the Coulomb interaction of the jumping particle with all other particles. For the calculation of $\Delta E_{\mathrm{c}}$ one has to take care of the image charges caused by the periodic boundary conditions, which is done by using Ewald's method ([48], see also Chap. 16). After each elementary step, the time $t$ is incremented by $\tau_0/N$, where $\tau_0 = \tau_\infty \exp(V_0/k_{\mathrm{B}}T)$ is the mean residence time between two jumps of an ion in the absence of Coulomb interactions and structural disorder (see Sect. 20.2).

Initially the particles are randomly distributed over the system. In order to reach a thermalized state at the final simulation temperature, the system is cooled down from a high temperature, $k_{\mathrm{B}}T = 10 \max\{\sigma_\epsilon, V_{\mathrm{c}}\}$, to the simulation temperature by a linear increase of $1/T$. After the cooling process, the temperature is held constant for a time equal to the cooling time; then the quantities of interest are determined. The time for the thermalization process is chosen such that the mean total energy of the ion system does not change significantly during the constant temperature phase, and is typically 3 to 5 times larger than the simulation time itself.

To obtain the mean square displacement $\langle r^2(t) \rangle$, all particle positions $\boldsymbol{r}_i(0)$ are stored at time $t = 0$ after thermalization. At time $t$, the particles are at positions $\boldsymbol{r}_i(t)$, and the mean square displacement is calculated from $\langle r^2(t) \rangle = (1/N) \sum_{i=1}^{N} [\boldsymbol{r}_i(t) - \boldsymbol{r}_i(0)]^2$. To obtain the SLR correlation functions $G^{(q)}(t)$, the magnetic field $\boldsymbol{B}$ is aligned along the $z$-direction and all pair vectors $\boldsymbol{r}_{ij}(0)$ are stored at time $t = 0$ using the minimum image convention [48]. At time $t$ these pair vectors are $\boldsymbol{r}_{ij}(t)$, and the $G^{(q)}(t)$ are calculated according to (20.15).

The frequency dependent conductivity is determined by the current response to a (small) external sinusoidal electric field $E(t) = E_0 \sin(\omega t)$ aligned in the $x$-direction. The effect of the field is taken into account by the way the neighboring site is chosen to which an ion attempts to jump (see above). In the absence of the electric field, the 6 nearest neighbor sites are equivalent and are chosen with equal probability $1/6$. In the presence of the field, the sites in the $\pm x$-direction are chosen with probability $(1 \pm \epsilon(t))/6$, where $\epsilon(t) \equiv eE(t)a/2k_{\mathrm{B}}T \ll 1$. The resulting current density $j_x(t)$ in the $x$-direction is determined by counting the number $N_+(t)$ and $N_-(t)$ of jumps in the $+x$- and $-x$-direction in a small time interval $t - \Delta t/2 \leq t < t + \Delta t/2$, where $\Delta t \ll 2\pi/\omega$. The mean values of $N_+(t)$ and $N_-(t)$, averaged over several samples, determine the mean current density $j_x(t) = ea(\langle N_+(t)\rangle - \langle N_-(t)\rangle)/L^3$ and, since $j_x(t)$ can be written as $j_x(t) = \sigma'(\omega)E_0 \sin(\omega t) - \sigma''(\omega)E_0 \cos(\omega t)$, the real and imaginary part $\sigma'(\omega)$ and $\sigma''(\omega)$ of the frequency dependent conductivity. In order to improve the statistics, the results are finally averaged over typically 100 thermalized configurations.

## 20.4 Dispersive Transport

For model I, most of our numerical simulations have been performed on a simple cubic lattice of length $L = 39a$, fixed ion density $c = 10^{-2}$ and fixed $\eta = e^2/(r_{\mathrm{s}}V_0) = 5$, which defines our set of standard parameters. $V_0$ denotes the structural potential barrier. To investigate the effect of percolative disorder, we compare results for the ordered lattice ($p = 1$) with those for the disordered substrate ($p = 0.4$). The strength of the Coulomb interactions, represented by the plasma parameter $\Gamma$, is varied by changing the temperature.

Figures 20.1 (a) and (b) show the time dependent diffusion coefficient $D(t) \equiv \langle r^2(t)\rangle/2dt$ in units of $D_0 \equiv a^2/2d\tau_0$ as a function of $t/\tau_0$ for $\Gamma = 0$, 40, and 80 in (a) the ordered lattice ($p = 1$) and (b) the disordered system ($p = 0.4$). For $t/\tau_0 \ll 1$, $\langle r^2(t)\rangle$ is proportional to the total number of successful hops, which increases linearly with time and therefore $D(t)$ is constant, $D(t) = D_{\mathrm{st}}$. For $t/\tau_0 > 1$, $D(t)$ decreases with time $t$ and finally approaches $D_{\mathrm{tr}}$. In the ordered system, the decrease of $D(t)$ is comparatively weak, even at large plasma parameters $\Gamma$ (low temperatures), while in the disordered system, $D(t)$ decreases over several orders of magnitude for large $\Gamma$. This behavior is reflected in the temperature dependence of the tracer correlation factor $f_{\mathrm{tr}}(\Gamma) = D_\infty/D_{\mathrm{st}}$ shown in Fig. 20.1 (c). In both the ordered and the disordered system, $f_{\mathrm{tr}}$ is thermally activated, $f_{\mathrm{tr}}(\Gamma) = f_{\mathrm{tr}}(0)\exp(-\Delta E_{\mathrm{f}}/k_{\mathrm{B}}T)$, but the activation energy $\Delta E_{\mathrm{f}}$ being the difference between the activation energies for the long and short time diffusion coefficients, is much larger in the disordered system ($\Delta E_{\mathrm{f}} = 0.05e^2/r_{\mathrm{s}} = 0.27V_0$) than in the ordered one ($\Delta E_{\mathrm{f}} = 0.01e^2/r_{\mathrm{s}} = 0.06V_0$). We conclude that in order to obtain strong
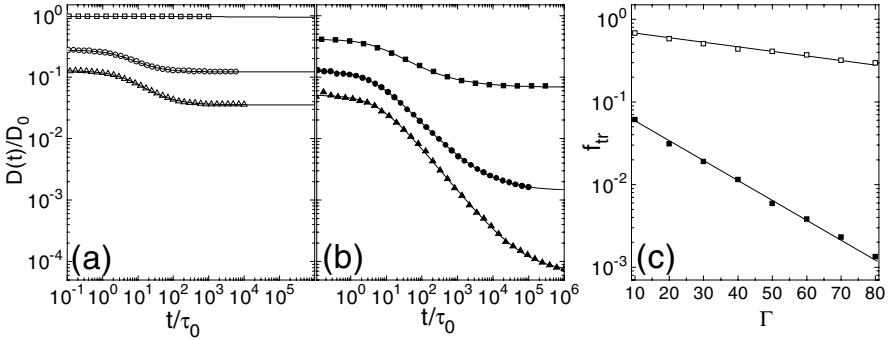
**Fig. 20.1.** Plot of (a) $D(t)$ in the ordered lattice for $\Gamma = 0$ ($\square$), 40 ($\circ$), and 80 ($\triangle$), (b) $D(t)$ in the disordered system (model I) for $\Gamma = 0$ ($\blacksquare$), 40 ($\bullet$), and 80 ($\blacktriangle$), and (c) the tracer correlation factor as a function of the plasma parameter $\Gamma$ in the ordered lattice ($\square$) and in the disordered system ($\blacksquare$). The full lines in (a) and (b) are least-square fits according to (20.21).

dispersion in the diffusive transport, we need both Coulomb interactions *and* structural disorder. In the following we will concentrate on this relevant case only and consider the curves shown in Fig. 20.1 (b) in more detail.

For $\Gamma \geq 20$, an intermediate time regime $t_1 < t < \tau_{\mathrm{D}}$ occurs, where $D(t)$ shows approximate power law behavior,

$$D(t) \sim t^{-n_{\mathrm{D}}}, \quad t_1 < t < \tau_{\mathrm{D}}. \tag{20.20}$$

The upper crossover time $\tau_{\mathrm{D}}$ and the exponent $n_{\mathrm{D}}$ increase with increasing $\Gamma$ (decreasing temperature), while the lower crossover time $t_1$ is approximately independent of $\Gamma$ and of the order of the inverse hopping rate $a^2/6D_{\mathrm{st}}$. The whole time dependence of $D(t)$ can be well described by the formula

$$D(t) = D_\infty + (D_{\mathrm{st}} - D_\infty) \left(1 + \frac{t}{t_1}\right)^{-n_{\mathrm{D}}}, \tag{20.21}$$

which has been suggested earlier by Funke on the basis of his jump relaxation model [11].

From the Nernst-Einstein relation (20.9) we expect that the power law behavior of $D(t)$ at intermediate time scales is reflected in a power law behavior of $\hat{\sigma}(\omega)$ at intermediate frequency scales, $1/\tau_{\mathrm{D}} < \omega < 1/t_1$. To determine $\hat{\sigma}(\omega)$ we have studied the current response to an external electric field $E(t) = E_0 \sin(\omega t)$ as described in Sect. 20.3. Figure 20.2 shows the real and imaginary parts $\sigma'(\omega)$ and $\sigma''(\omega)$ of the conductivity $\hat{\sigma}(\omega)$ in units of $\sigma_0 \equiv e^2/2k_{\mathrm{B}}Ta\tau_0$ as a function of $\omega\tau_0$ for (a) $\Gamma = 0$, (b) $\Gamma = 40$ and (c) $\Gamma = 80$.

For comparison we show also the real and imaginary parts of $\hat{\sigma}_{\mathrm{D}}(\omega) \equiv \rho e^2 \hat{D}(\omega)/k_{\mathrm{B}}T$ (full lines in the figure), which one obtains for the complex
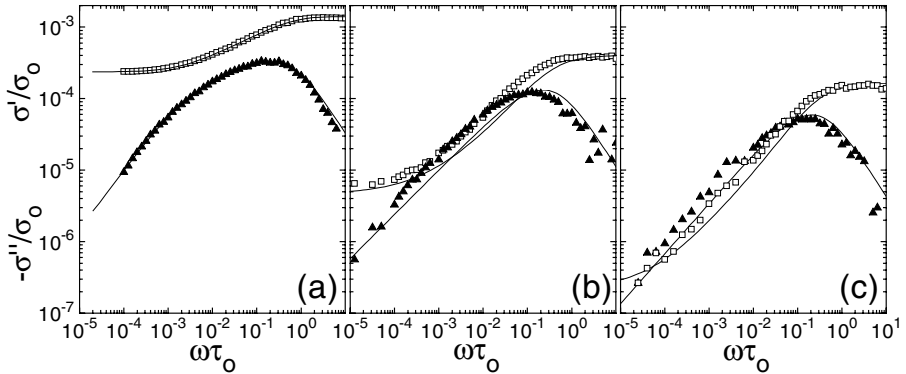
**Fig. 20.2.** Real ($\square$) and imaginary part ($\blacktriangle$) of the conductivity in model I for (a) $\Gamma = 0$, (b) $\Gamma = 40$, and (c) $\Gamma = 80$. The full lines are explained in the text.

conductivity when neglecting the cross-correlations in the autocorrelation function of the current density in (20.8). The frequency dependent tracer diffusion coefficient $\hat{D}(\omega)$ is obtained numerically by a Laplace transform of $\langle r^2(t) \rangle$ (see (20.6)). Since $\sigma''(\omega) \leq 0$, we have plotted $-\sigma''(\omega)$ in the figure. For $\Gamma = 0$, $\hat{\sigma}(\omega)$ and $\hat{\sigma}_D(\omega)$ coincide, since in this case the cross-correlations practically vanish (the effect of the hard-core interaction between the mobile ions can be neglected since $c = 0.01$ is very small). For $\Gamma = 40$ and 80, $\hat{\sigma}(\omega)$ and $\hat{\sigma}_D(\omega)$ are equal at high frequencies, but deviate at lower frequencies. Despite this, the overall behavior is quite similar. Both $\sigma'(\omega)$ and $\sigma'_D(\omega)$ exhibit a dc plateau at low frequencies $\omega \ll 1/t_2$ and approach $\sigma_\infty = \rho e^2 D_{st}/k_B T$ at high frequencies $\omega \gg 1/t_1$. In between they can be approximately described by

$$\sigma'(\omega) \sim (\omega\tau_0)^{n_\sigma}, \quad \tau_0/\tau_\sigma \ll \omega\tau_0 \ll \tau_0/t_1, \tag{20.22}$$

where $n_\sigma = n_D$ and $\tau_\sigma \approx \tau_D$. At very high frequencies the conductivity becomes constant again. This high frequencies plateau is difficult to detect experimentally, especially in glasses, because dynamical processes not included in the lattice gas model, e.g. vibrations of the glassy matrix, become dominant (see however [49]). In some crystalline ion conductors as e.g. $RbAg_4I_5$ or Na-$\beta''$-Alumina, however, a high frequency plateau was found ([3], Chap. 23).

Since the cross-correlations do not affect strongly the overall behavior of $\sigma(\omega)$ one can hope to understand the origin of the conductivity dispersion from the behavior of the time dependent tracer diffusion coefficient. Indeed, to map the complex dynamics of the many-particle system to an effective dynamics of a one-particle system, it has been suggested that the mutual interactions between the ions can be described by an effective distribution $\psi(\tau_w)$ of waiting times $\tau_w$ between successive jumps of a tracer particle. This continuous time random walk model (CTRW) (see e.g. [50]) was proposed by
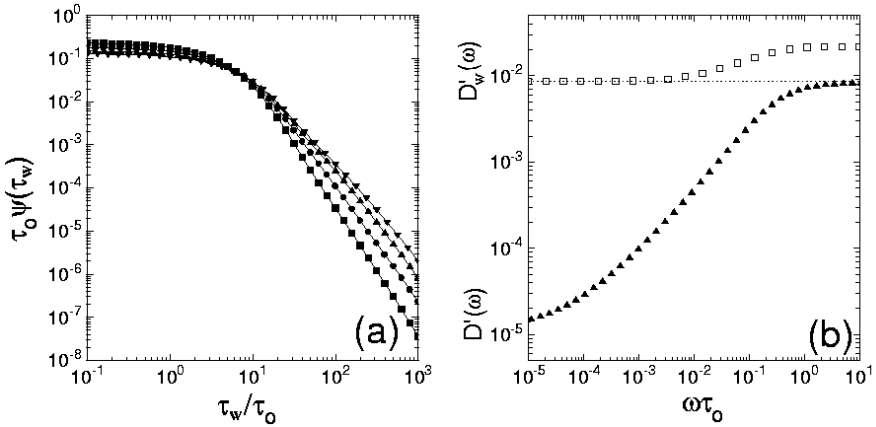
**Fig. 20.3.** Plot for model I of (a) the distribution function of the waiting time $\tau_w$ between successive jumps as a function of $\tau_w/\tau_0$ for different plasma parameters, $\Gamma = 20$ (■), 40 (●), 60 (▲) and 80 (▼), and (b) the real part of the diffusion coefficient $D'_{\mathrm{w}}(\omega)/D_0$ (obtained from the approximation (20.23)) (□) and the correct $D'(\omega)/D_0$ (obtained from (20.6)) (▲) for $\Gamma = 80$.

Scher and Lax [51] to describe the dielectric response of amorphous semiconductors.

To test if the CTRW model applies here, we have determined the number $N(\tau_{\mathrm{w}})$ of waiting times $\tau'_{\mathrm{w}}$ between two successive jumps of a tracer particle, which lie in the interval $\tau_{\mathrm{w}} - \Delta\tau_{\mathrm{w}} \leq \tau'_{\mathrm{w}} < \tau_{\mathrm{w}} + \Delta\tau_{\mathrm{w}}$. The waiting time distribution $\psi(\tau_{\mathrm{w}})$ is related to $N(\tau_w)$ by $\psi(\tau_{\mathrm{w}}) = AN(\tau_{\mathrm{w}})/2\Delta\tau_{\mathrm{w}}$, where the prefactor $A$ follows from the normalization condition, $\int_0^\infty d\tau_{\mathrm{w}}\psi(\tau_{\mathrm{w}}) = 1$. Figure 20.3 (a) shows $\psi(\tau_{\mathrm{w}})$ times $\tau_0$ as a function of $\tau_{\mathrm{w}}/\tau_0$ for various plasma parameters $\Gamma$. For all values of $\Gamma$, $\tau_0\psi(\tau_{\mathrm{w}}) \simeq 10^{-1}$ is approximately constant for $\tau_{\mathrm{w}}/\tau_0 < 1$ and decreases rapidly for $\tau_{\mathrm{w}}/\tau_0 > 10$. As one would expect, the decrease is weaker for larger $\Gamma$, but no significant change of $\psi(\tau_{\mathrm{w}})$ occurs if $\Gamma$ is increased.

The one-sided Fourier transform of the waiting time distribution $\psi(\tau_{\mathrm{w}})$ is (within the CTRW model) related to the frequency dependent diffusion coefficient $\hat{D}_{\mathrm{w}}(\omega)$ by [51]

$$\hat{D}_{\mathrm{w}}(\omega) = \frac{a^2}{6}\frac{\mathrm{i}\omega\hat{\psi}(\omega)}{1 - \hat{\psi}(\omega)}. \tag{20.23}$$

In Fig. 20.3 (b) we compare $D'_{\mathrm{w}}(\omega)/D_0$ (obtained from (20.23)) with the correct $D'(\omega)/D_0$ (obtained from (20.6)) for $\Gamma = 80$. The two curves are completely different: In contrast to $D'(\omega)$, $D'_{\mathrm{w}}(\omega)$ shows only a very weak dispersion. The *low*-frequency limit of $D'_{\mathrm{w}}(\omega)$ is the same as the *high*-frequency limit of $D'(\omega)$.
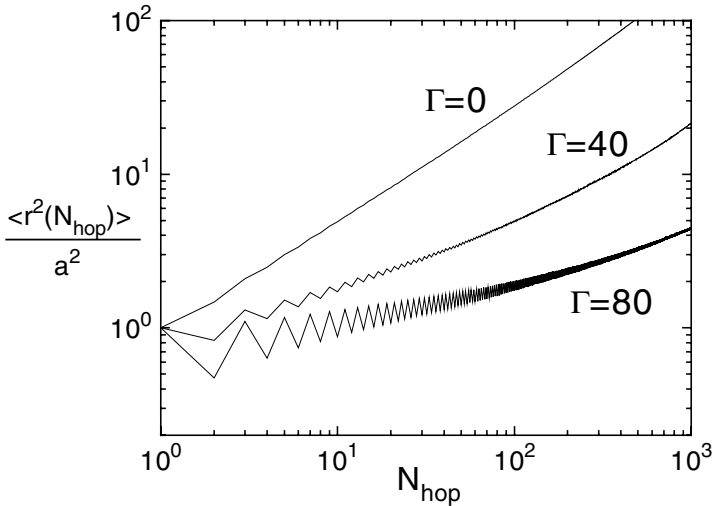
**Fig. 20.4.** Mean square displacement $\langle r^2(N_{\mathrm{hop}})\rangle$ as a function of the number of performed hops $N_{\mathrm{hop}}$ for different plasma parameters $\Gamma$.

These deviations show clearly the principle difficulties of the CTRW-model (see also [52]). If the initial waiting time $\tau_{\mathrm{w}}^0$, the tracer particle needs for the first jump, is chosen according to the proper stationary distribution, $\psi_0(\tau_{\mathrm{w}}^0) = \int_0^\infty d\tau_{\mathrm{w}}\psi(\tau_{\mathrm{w}}^0 + \tau_{\mathrm{w}})/\int_0^\infty d\tau_{\mathrm{w}}^0 \int_0^\infty d\tau_{\mathrm{w}}\psi(\tau_{\mathrm{w}}^0 + \tau_{\mathrm{w}})$, then $D(\omega)$ shows no dispersion at all, $D(\omega) = D_{st}$ just as in the simple random walk case. The larger value of $D_{\mathrm{w}}$ at high frequencies is an artifact of the CTRW-model and results from the fact that the initial time $\tau_{\mathrm{w}}^0$ is assumed to be distributed according to $\psi$ rather than to the stationary distribution.

Since the time inhomogeneities in the tracer motion can not be responsible for the dispersion, we now study spatial correlations in the tracer trajectory. We consider the mean square displacement $\langle r^2(N_{\mathrm{hop}})\rangle$ as a function of the number of performed hops $N_{\mathrm{hop}}$, which is shown in Fig. 20.4 for various plasma parameters $\Gamma$. At $N_{\mathrm{hop}} = 1$, $\langle r^2(N_{\mathrm{hop}})\rangle/a^2 = 1$ for all $\Gamma$ since a tracer particle has moved the distance $a$ after the first jump. At small plasma parameters, $\langle r^2(N_{\mathrm{hop}})\rangle$ increases monotonously with $N_{\mathrm{hop}}$. At larger values of $\Gamma$ ($\Gamma \geq 20$), a striking alternation of $\langle r^2(N_{\mathrm{hop}})\rangle$ for even and odd $N_{\mathrm{hop}}$ begins to emerge for $1 < N_{\mathrm{hop}} < N_{\mathrm{hop}}^{(2)}$, which becomes more pronounced at larger $\Gamma$. The upper crossover number $N_{\mathrm{hop}}^{(2)}$ increases with increasing $\Gamma$ and is of the order of the product of the jump rate $6D_{st}/a^2$ and the crossover time $t_2 \approx \tau_\sigma$, $N_{\mathrm{hop}}^{(2)} \simeq 6D_{st}t_2/a^2$. For even values of $N_{\mathrm{hop}}$, $\langle r^2(N_{\mathrm{hop}})\rangle$ shows approximate power law behavior

$$\langle r^2(2N_{\mathrm{hop}})\rangle \sim (2N_{\mathrm{hop}})^k, \quad 1 < N_{\mathrm{hop}} < N_{\mathrm{hop}}^{(2)}, \tag{20.24}$$

where $k = 1 - n_{\mathrm{D}} = 1 - n_\sigma$ is the exponent expected from the behavior of $\langle r^2(t) \rangle$, if $t$ is simply replaced by the average time $2N_{\mathrm{hop}}/6D_{\mathrm{st}}$ after $2N_{\mathrm{hop}}$ jumps of the tracer particle, $\langle r^2(2N_{\mathrm{hop}}) \rangle \simeq \langle r^2(t = 2N_{\mathrm{hop}}/6D_{\mathrm{st}}) \rangle$.

The striking alternation of $\langle r^2(N_{\mathrm{hop}}) \rangle$ is caused by strong forward-backward correlations in the tracer motion, which occurs on length scales of the order of the lattice constant $a$. Before its first jump the tracer ion finds itself in a deep energy minimum, which is created by the surrounding ions. After its first jump the ion is in an energetically unfavourable situation and has a large tendency to jump back to the original site. Thus $\langle r^2(N_{\mathrm{hop}} = 2) \rangle < \langle r^2(N_{\mathrm{hop}} = 1) \rangle = a^2$. Repetition of these forward-backward jumps leads to the alternating behavior of $\langle r^2(N_{\mathrm{hop}}) \rangle$. Sometimes it happens that an energetically unfavourable position is stabilized by jump relaxation processes of the surrounding ions. This causes $\langle r^2(N_{\mathrm{hop}}) \rangle$ to increase slightly, but the increase is much weaker than in the absence of the forward-backward correlations. The presence of disorder is important for the forward backward correlations to arise because the surrounding ions cannot follow the tracer ion without making detours, which delays the local relaxation process considerably. A similar suppression of the mobility of the surrounding ion cloud can be expected to occur in ordered lattices by a complex lattice structure with several sites per unit cell, as, for example, in the crystalline superionic conductor RbAg$_4$I$_5$. In ordered Bravais lattices, the surrounding ions can easily stabilize the position of the tracer ion and the forward-backward correlations are very small. The forward-backward correlations dominate the overall behavior on a length scale of the lattice constant. When $\langle r^2(N_{\mathrm{hop}}) \rangle^{1/2}$ has reached a few lattice constants at $N_{\mathrm{hop}} \gg N_{\mathrm{hop}}^{(2)}$, the effect ceases to be dominant and the dispersion becomes considerably weaker.

In order to understand why the even values of $N_{\mathrm{hop}}$ between 1 and $N_{\mathrm{hop}}^{(2)}$ determine the behavior of $\langle r^2(t) \rangle$ between $t_1 \simeq 1/6D_{\mathrm{st}}$ and $t_2 \simeq N_{\mathrm{hop}}^{(2)}/6D_{\mathrm{st}}$, one must be aware that for a fixed time $t$ the probability that the tracer ion has performed an even number of jumps is much larger than the probability that it has performed an odd number of jumps. After an odd number of jumps the tracer ion mostly finds itself in an energetically unfavourable position and stays there only for a short time (compared to the time spent on a site after an even number of jumps). Hence the probability that a particle has performed an odd number of jumps at a given time $t$ is small, and does not contribute to the mean square displacement at $t$.

The forward-backward correlations also cause characteristic changes of the distribution function $P(\boldsymbol{r}, t)$ and its Fourier transforms. Fig. 20.5 (a) shows $\log(P(\boldsymbol{r}, t)/P(0, t))$ as a function of the scaled distance $r/R(t)$, where $R(t) = \langle r^2(t) \rangle^{1/2}$ is the root mean square displacement, in the disordered system for $\Gamma = 40$ and 80, and several times $t$ in the dispersive regime. It is remarkable that although $R(t)$ is small in this regime, the curves collapse, showing that the simple scaling relation $P(\boldsymbol{r}, t)/P(0, t) = f(r/R(t))$ holds as in the simple random walk case. For $\Gamma = 40$ and 80, the scaling function $f(x)$ is no longer

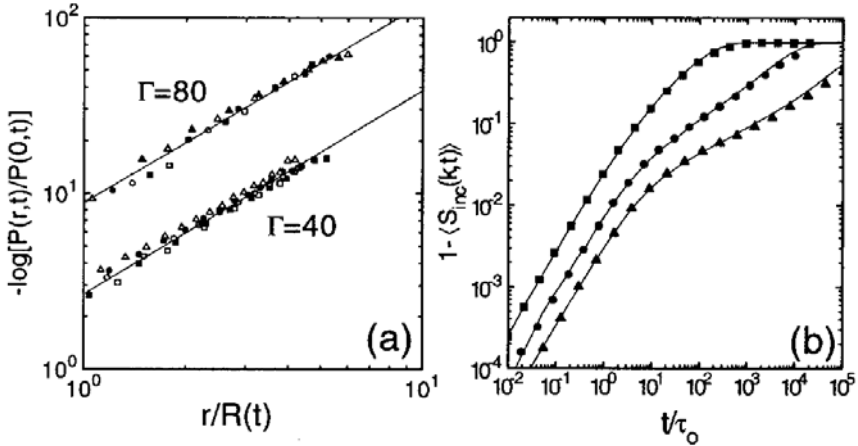**Fig. 20.5.** Plot of (a) the distribution function $\log(P(\boldsymbol{r},t)/P(0,t))$ versus $r/R(t)$ in the disordered system I ($p = 0.4$) for $\Gamma = 40$ and 80, and (b) of $1 - \tilde{S}_{\mathrm{inc}}(k,t)$ for $k = 2\pi/10a$ as a function of $t/\tau_0$. In (a) different symbols refer to different times: For $\Gamma = 40$: $t/\tau_0 = 546$ ($\square$), 1130 ($\blacksquare$), 2340 ($\circ$), 4830 ($\bullet$), and 10000 ($\triangle$) and for $\Gamma = 80$: $t/\tau_0 = 113$ ($\square$), 264 ($\blacksquare$), 616 ($\circ$), 1440 ($\bullet$), 3360 ($\triangle$), and 7850 ($\blacktriangle$). The data points for $\Gamma = 80$ have been multiplied by a factor of 4. In (b) different symbols refer to different plasma parameters $\Gamma = 0$ ($\blacksquare$), 40 ($\bullet$), and 80 ($\blacktriangle$), and the full lines are the approximation (20.26).

a Gaussian, but a stretched Gaussian, $f(x) = \exp(-cx^u)$, with $u \simeq 1.2$. For $\Gamma = 0$ in contrast, $P(\boldsymbol{r},t)$ shows the expected scaling behavior with a Gaussian scaling function only at larger times (Fig. 20.5 (b)). It is interesting to note that the exponent $u$ satisfies the relation

$$u = \frac{2}{1 + n_{\mathrm{D}}} \quad , \tag{20.25}$$

which has been originally derived to describe the distribution function of random walks on random fractal structures [53].

In order to discuss the Fourier transform of $P(\boldsymbol{r},t)$, the intermediate scattering function, we first remove any artificial effects of the lattice anisotropy by averaging $S_{\mathrm{inc}}(\boldsymbol{k},t)$ over the $\boldsymbol{k}$-vector orientation $\tilde{S}_{\mathrm{inc}}(k,t) \equiv (4\pi)^{-1} \int d\Omega \, S_{\mathrm{inc}}(\boldsymbol{k},t)$. For $kR(t) \ll 1$ and $R(t) \ll 1$ it is easy to verify that $\tilde{S}_{\mathrm{inc}}(k,t)$ can be approximated by

$$\tilde{S}_{\mathrm{inc}}(k,t) \simeq \exp(-\frac{k^2 R^2(t)}{6}). \tag{20.26}$$

Fig. 20.5 (b) shows $1 - \tilde{S}_{\mathrm{inc}}(k,t)$ for $k = 2\pi/10a$ and $\Gamma = 0$, 40, and 80. Quite surprisingly, the simple approximation (20.26) holds in the whole decay regime, showing that the decay changes from a simple to a stretched exponential when $\Gamma$ becomes larger (see also [11]).
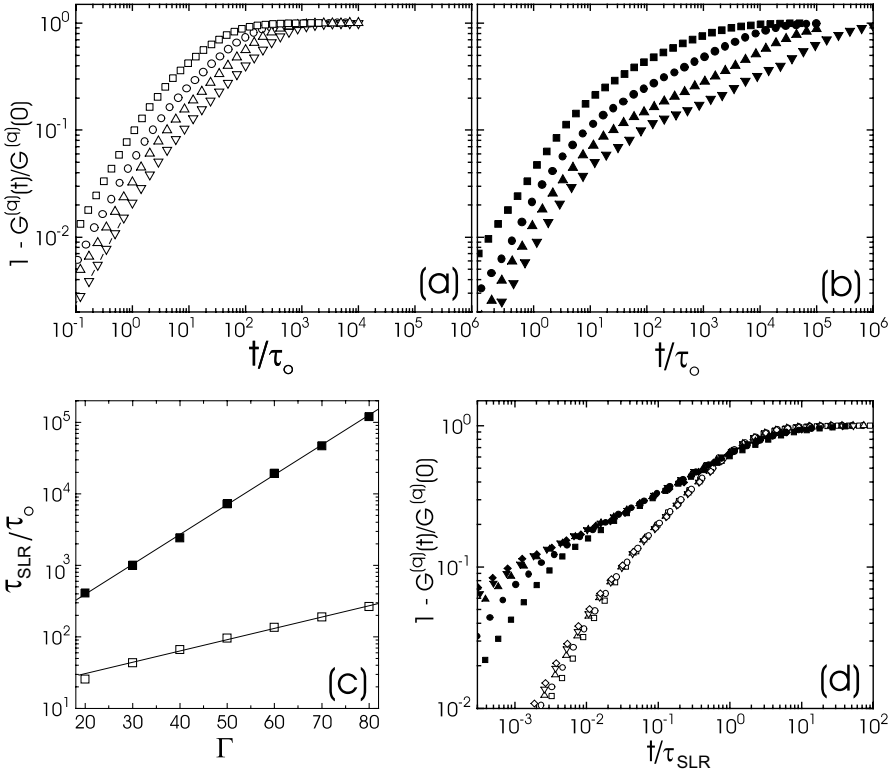
**Fig. 20.6.** Plot of $1 - G^{(2)}(t)/G^{(2)}(0)$ in model I (a) as a function of $t/\tau_0$ for $p = 1$ and $\Gamma = 20$ ($\square$), 40 ($\circ$), 60 ($\triangle$) and 80 ($\triangledown$), (b) as a function of $t/\tau_0$ for $p = 0.4$ and $\Gamma = 20$ ($\blacksquare$), 40 ($\bullet$), 60 ($\blacktriangle$) and 80 ($\blacktriangledown$). Part (c) shows the correlation time $\tau_{\mathrm{SLR}}$ for $p = 1$ ($\square$) and $p = 0.4$ ($\blacksquare$) as a function of $\Gamma$, and part (d) $1 - G^{(2)}(t)/G^{(2)}(0)$ as a function of the scaling parameter $t/\tau_{\mathrm{SLR}}$ for $p = 1$ (open symbols), $p = 0.4$ (full symbols) and $\Gamma = 40$ ($\square,\blacksquare$), 50 ($\circ,\bullet$), 60 ($\triangle,\blacktriangle$), 70 ($\triangledown,\blacktriangledown$) and 80 ($\lozenge,\blacklozenge$).

Next we discuss the SLR correlation functions $G^{(q)}(t)$, $q = 1, 2$. We again compare our results for the ordered lattice ($p = 1$) and the disordered substrate ($p = 0.4$). For sufficiently large values of $\Gamma$ ($\Gamma > 1$) the distribution of the mobile ions is isotropic and therefore $G^{(2)}(0) = 4G^{(1)}(0)$ [43]. Numerically we find that for $\Gamma > 10$, $G^{(2)}(t) \cong 4G^{(1)}(t)$ is valid for all times $t$, and thus $G^{(2)}(t)/G^{(2)}(0) \equiv G^{(1)}(t)/G^{(1)}(0)$. Since the $G^{(q)}(t)$ decay faster than $1/t$ for very long times, the asymptotics is irrelevant for $1/T_1$ (see the discussion above, Sect. 20.2.4), and the relevant decay regime is most conveniently discussed in terms of the functions $1 - G^{(q)}(t)/G^{(q)}(0)$, which are shown in Fig. 20.6. Both in the ordered lattice (Fig. 20.6 (a)) and the disordered system (Fig. 20.6 (b)), $1 - G^{(q)}(t)/G^{(q)}(0)$ are proportional to $t/\tau_0$ for small $t/\tau_0$ values. Similar as in the diffusion coefficient, an intermediate time regime can be well identified in the disordered system for $\Gamma > 20$, where
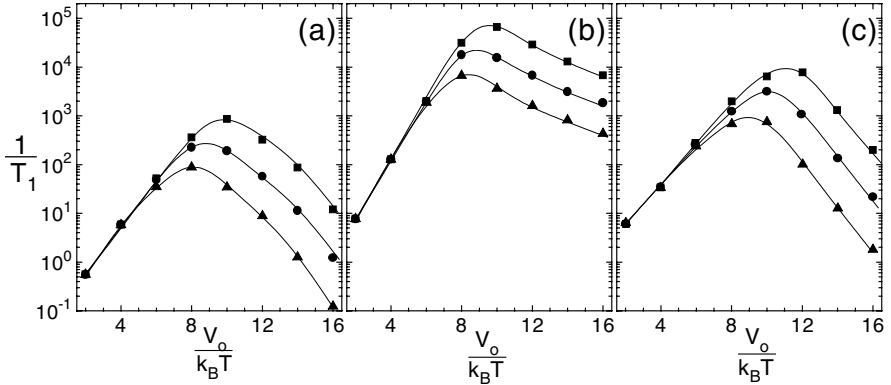
**Fig. 20.7.** Spin-lattice relaxation rate $1/T_1$ in units of $C\tau_\infty$ as a function of $V_0/k_BT$ for (a) $p = 1$ and $\eta = 5$ (ordered system with Coulomb interaction), (b) $p = 0.4$ and $\eta = 5$ (disordered system with Coulomb interaction), and (c) $p = 0.4$ and $\eta = 0$ (disordered system without Coulomb interaction). Different symbols denote different frequencies. In (a) $\omega_L\tau_\infty = 3\cdot10^{-7}$ (■), $9.5\cdot10^{-7}$ (●) und $3\cdot10^{-6}$ (▲), in (b) $\omega_L\tau_\infty = 3\cdot10^{-9}$ (■), $9.5\cdot10^{-9}$ (●) und $3\cdot10^{-8}$ (▲), and in (c) $\omega_L\tau_\infty = 3\cdot10^{-6}$ (■), $9.5\cdot10^{-6}$ (●) und $3\cdot10^{-5}$ (▲).

$1 - G^{(q)}(t)/G^{(q)}(0) \sim (t/\tau_0)^{1-n_{\mathrm{SLR}}}$. The exponent $n_{\mathrm{SLR}}$ is independent of temperature, $n_{\mathrm{SLR}} \cong 0.73$. In the ordered lattice, the decay of the $G^{(q)}(t)$ is much faster and a corresponding intermediate time interval is hardly seen.

Figure 20.6 (c) shows the SLR correlation time $\tau_{\mathrm{SLR}}$, which we define as the time, where $G^{(q)}(t)$ has decreased to $1/e$ of its initial value, i.e. $G^{(q)}(\tau_{\mathrm{SLR}})/G^{(q)}(0) = 1/e$. Due to strong correlations in the ionic motion, $\tau_{\mathrm{SLR}}$ is stronger activated than $\tau_0$, $\tau_{\mathrm{SLR}}/\tau_0 = \exp(\Delta E_{\mathrm{SLR}}/k_BT)$, $\Delta E_{\mathrm{SLR}} \equiv E_{\mathrm{SLR}} - V_0 > 0$. The activation energy $\Delta E_{\mathrm{SLR}}$ is smaller in the ordered lattice ($\Delta E_{\mathrm{SLR}} \cong 0.04e^2/r_s = (0.04\eta V_0)$) than in the disordered system ($\Delta E_{\mathrm{SLR}} \cong 0.09e^2/r_s = (0.09\eta V_0)$), where $\tau_{\mathrm{SLR}}$ exceeds $\tau_0$ by more than 5 orders of magnitude for $\Gamma = 80$.

Fig. 20.6 (d) shows $1 - G^{(q)}(t)/G^{(q)}(0)$ as a function of $t/\tau_{\mathrm{SLR}}$. The data collapse shows that on time scales larger than $\tau_0$, $G^{(q)}(t)/G^{(q)}(0)$ is only a function of $t/\tau_{\mathrm{SLR}}$ (independent of $\Gamma$), in particular $1 - G^{(q)}(t)/G^{(q)}(0) \sim (t/\tau_{\mathrm{SLR}})^{1-n_{\mathrm{SLR}}}$ for $\tau_0/\tau_{\mathrm{SLR}} \ll t/\tau_{\mathrm{SLR}} < 1$. Accordingly in the relevant decay regime, the correlation functions can be approximately written in KWW form, $G^{(q)}(t) = G^{(q)}(0)\exp(-(t/\tau_{\mathrm{SLR}})^{1-n_{\mathrm{SLR}}})$, in the relevant regime.

With (20.13) we obtain $1/T_1(\omega_L,T)$ by Fourier transformation. Figure 20.7 shows $1/T_1(\omega,T)$ as a function of $V_0/k_BT$ for $\eta = 5$ and various Larmor frequencies $\omega_L$ in (a) the ordered lattice, and (b) the disordered system. For comparison, we show in (c) also the behavior of $1/T_1$ for uncharged particles ($\eta = 0$, $\Gamma \equiv 0$) diffusing in the disordered system. Since in all cases (a)–(c), the $G^{(q)}(t)$ decay faster than $1/t$ for large times, $1/T_1$ is independent of $\omega_L$ at the high temperature side of the maximum. For the uncharged par-
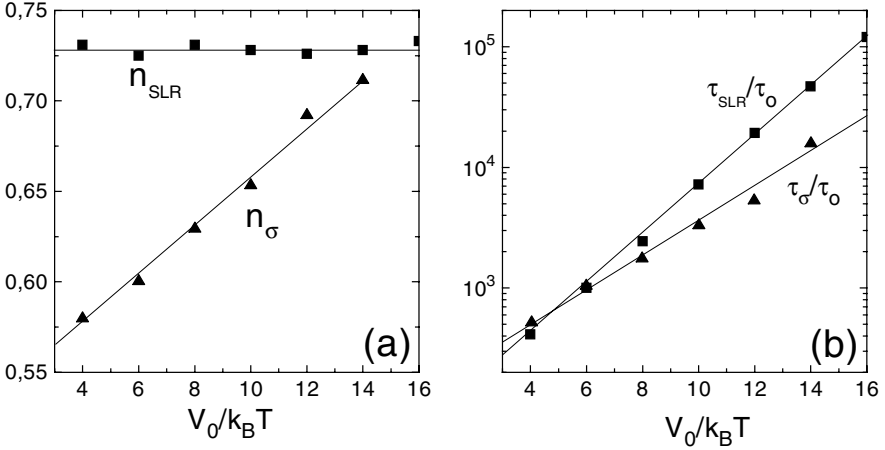
**Fig. 20.8.** Plot of (a) the exponents $n_\sigma$ and $n_{\mathrm{SLR}}$ and (b) the correlation times $\tau_\sigma/\tau_0$ and $\tau_{\mathrm{SLR}}/\tau_0$ as a function of $V_0/k_\mathrm{B}T$ for $p = 0.4$ and $\eta = 5$.

ticles (Fig. 20.7 (c)), $1/T_1$ shows no significant deviation from the standard BPP behavior. For charged particles slight deviations occur in the ordered lattice (Fig. 20.7 (a)), but the typical non-BPP behavior according to (20.5) does not occur. The deviations predominantly show up in a weak asymmetry of $1/T_1$ near the maximum. In case (b), when both disorder and Coulomb interactions are present, we obtain the typical non-BPP behavior: The curves are asymmetric in shape, the maximum occurs at $\omega_\mathrm{L}\tau_{\mathrm{SLR}} \approx 1 \gg \omega_\mathrm{L}\tau_0$ (note that this relation is the only way to experimentally determine $\tau_{\mathrm{SLR}}$ as a function of $T$), and $1/T_1$ decreases as $1/T_1 \sim \tau_0(\omega_\mathrm{L}\tau_0)^{n_{\mathrm{SLR}}-2}$ at low temperatures ($\omega_\mathrm{L} \gg 1/\tau_{\mathrm{SLR}}$). The activation energies are $E_1^{\mathrm{SLR}} \cong 1.5V_0$ and $E_2^{\mathrm{SLR}} \cong 0.4V_0$. Since $E_{\mathrm{SLR}} \cong 1.45V_0$ for $\eta = 5$ (see above) also $E_{\mathrm{SLR}} \simeq E_1^{\mathrm{SLR}}$ is fulfilled. We conclude that, similar to our result for the conductivity $\sigma(\omega)$, both structural disorder and Coulomb interactions are needed to obtain qualitative agreement with the experimental findings. Again, we concentrate on this relevant case only.

As a consequence of the scaling behavior of $G^{(q)}(t)$, $1/T_1(\omega_\mathrm{L}, T)$ obeys the simple scaling relation

$$\frac{1}{T_1}(\omega_\mathrm{L}, T) = \tau_{\mathrm{SLR}}g(\omega_\mathrm{L}\tau_{\mathrm{SLR}}), \qquad (20.27)$$

with $g(x) = $ const. for $x \ll 1$ and $g(x) \propto x^{n_{\mathrm{SLR}}-2}$ for $x \gg 1$. Equation (20.27) implies $E_1^{\mathrm{SLR}} = E_{\mathrm{SLR}}$ and the relation $E_2^{\mathrm{SLR}} = (1 - n_{\mathrm{SLR}})E_1^{\mathrm{SLR}}$ first proposed by Ngai [31].

Next we compare the exponent $n_{\mathrm{SLR}}$ and the correlation time $\tau_{\mathrm{SLR}}$ with the corresponding quantities in the conductivity spectra. Figure 20.8 (a) shows that $n_\sigma$ is smaller than $n_{\mathrm{SLR}}$ for $V_0/k_\mathrm{B}T < 16$ and seems to approach

$n_{\mathrm{SLR}}$ at lower temperatures. Only at these very low temperatures we expect mean field approaches [11] yielding $n_\sigma = n_{\mathrm{SLR}}$ to be applicable. From Fig. 20.8 (b) we find that the conductivity relaxation time $\tau_\sigma$ is less activated than the correlation time $\tau_{\mathrm{SLR}}$ in spin-lattice relaxation, and therefore $\tau_{\mathrm{SLR}}/\tau_\sigma \gg 1$ at lower temperatures. This is in accordance with experimental results for, e.g., $(\mathrm{LiCl})_{0.6}(\mathrm{Li_2O})_{0.7}(\mathrm{B_2O_3})_{1.0}$ [54], glassy $\mathrm{LiAl\,Si_2O_6}$ [55] and $\mathrm{LiAlSi_4O_{10}}$ [56], and flourozirconate glasses [7]. The reason for these differences is that although the phenomena observed in both experiments originate from the same ion transport mechanism, they are governed by *different* correlation functions: In spin-lattice relaxation, the correlation functions are determined by diffusion of ion pairs, while in conductivity the current correlation function is mainly determined by the diffusion of single ions.

## 20.5 Non-Arrhenius Behavior

In the preceding section, we have shown that simple percolative disorder and the Coulomb interaction between the ions can account for the typical anomalies found in several transport quantities. Another interesting effect is the non-Arrhenius behaviour of fast ion conducting glasses [20]. Clearly it would be desirable to confirm this effect also in tracer diffusion measurements [57].

In order to explain non-Arrhenius behaviour, one has to include the energy fluctuations associated with the disorder present in the material. To begin our discussion of energy fluctuations, we first assume non-interacting particles moving between lattice sites with energies drawn form a Gaussian distribution, as in model II, cf. (20.18). For that problem, the dc activation energy at low $T$ can be calculated analytically [33, 34]. Since double occupancy of sites is forbidden, the ions in equilibrium are distributed according to a Fermi distribution. At temperatures $T \ll \sigma_\epsilon/k_{\mathrm{B}}$, the activation energy follows from a critical percolation path argument [58, 59], $E_\sigma = \epsilon_{\mathrm{c}} - \epsilon_{\mathrm{f}}(c)$. Here $\epsilon_{\mathrm{f}}(c)$ is the Fermi energy, defined by $\int_{-\infty}^{\epsilon_{\mathrm{f}}} P(\epsilon)d\epsilon = c$, and $\epsilon_{\mathrm{c}}$ is the critical energy given by $\int_{-\infty}^{\epsilon_{\mathrm{c}}} P(\epsilon) = p_{\mathrm{c}}$, where $p_{\mathrm{c}}$ is the percolation threshold [45] in the sc-lattice, $p_{\mathrm{c}} \simeq 0.3117$. For $c = 0.01$ we obtain $E_\sigma = 1.84\sigma_\epsilon$. Because of the weak dependence of $\epsilon_{\mathrm{f}}$ on $c$ (see Sect. 20.7), $E_\sigma$ assumes similar values for other reasonable concentrations $c \ll 1$.

At high temperatures $T \gg \sigma_\epsilon/k_{\mathrm{B}}$, the conductivity is well approximated by $\sigma_{\mathrm{dc}} \simeq \sigma_{\mathrm{hf}} = \rho q^2 a^2 W_0/6k_{\mathrm{B}}T$. As can be shown by a high-temperature expansion, $W_0$ is given by $W_0 \simeq (1 - c)\mathrm{erfc}(\sigma_\epsilon/(2k_{\mathrm{B}}T)) \simeq (1 - c)\exp(-\sigma_\epsilon/\sqrt{\pi}k_{\mathrm{B}}T)$, in leading order of $\sigma_\epsilon/k_{\mathrm{B}}T$. Hence we obtain a high-temperature activation energy $E_0 = \sigma_\epsilon/\sqrt{\pi} \cong 0.56\sigma_\epsilon$ that is smaller than $E_\sigma$. Accordingly, the apparent activation energy $E(T)$ changes from $E_\sigma$ for low temperatures to $E_0$ at a crossover temperature $T_x \simeq \sigma_\epsilon/k_{\mathrm{B}}$. Figure 20.9 (a) shows the simulation results for $\sigma_{\mathrm{dc}}$ (data points) in comparison
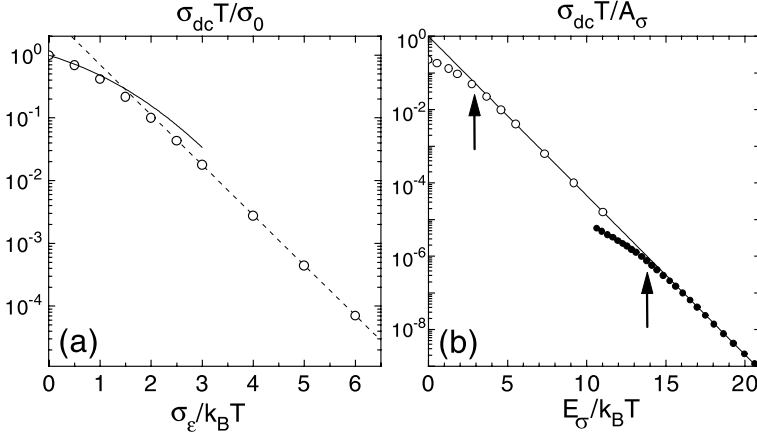
**Fig. 20.9.** Arrhenius plot of $\sigma_{dc}T$ for $V_c = 0$ and $c = 0.01$ (open circles) (a) in units of $\sigma_0$ as a function of $\sigma_\epsilon/k_BT$ and (b) in units of the preexponential factor $A_\sigma$ of the low-temperature Arrhenius law as a function of $E_\sigma/k_BT$. In (a) the full line shows the high temperature approximation (see text), the dashed line corresponds to $A_\sigma \exp(-E_\sigma/k_BT)$, where $E_\sigma = 1.84\sigma_\epsilon$ and $A_\sigma$ was taken to get the best fit to the data. For comparison, the experimental data for $0.4AgI+(0.6)[0.525Ag_2S+0.475(B_2S_3{:}SiS_2)]$ are shown in (b) (filled symbols, redrawn from [20]). The solid line is drawn as guide for the eye.

with the analytical results (lines). Except for the crossover regime $T \approx T_x$, the calculated activation energy agrees perfectly with the simulation data.

At first glance, the crossover at high temperatures seems to be very similar to recent experimental results for fast ion glasses [20]. Notice however, that both $E_\sigma$ and $k_BT_x$ are of the same order of magnitude, determined by $\sigma_\epsilon$. This is a serious disagreement to the experiments, where the non-Arrhenius behavior sets in at temperatures more than one order of magnitude smaller than $E_\sigma/k_B$. The disagreement can be seen clearly in Fig. 20.9 (b), where we have plotted both the simulation results in the absence of Coulomb interactions (open circles) and the experimental data (filled circles) [20] as a function of $E_\sigma/k_BT$. The arrows indicate the crossover temperatures and show that both disagree by about an order of magnitude.

Next we include the Coulomb interaction i. e. consider the complete model II, cf. (20.18). That model now is characterized by the typical interaction energy $V_c \equiv e^2/r_s$ and the disorder energy $\sigma_\epsilon$. Since we have found in Sect. 20.4 that the cross correlations give only a minor contribution to the conductivity, we have calculated the dc conductivity from the long-time limit of $D(t)$ by using (20.9) and neglecting the cross correlations. Figure 20.10 (a) shows $\sigma_{dc}T$ in units of $\sigma_0$ as a function of $V_c/k_BT$ for $c = 0.01$ and $\sigma_\epsilon/V_c = 0.0115$, 0.018, 0.036, and 0.072. At low temperatures, each curve follows a straight line corresponding to an Arrhenius law with constant activation energy $E_\sigma$,

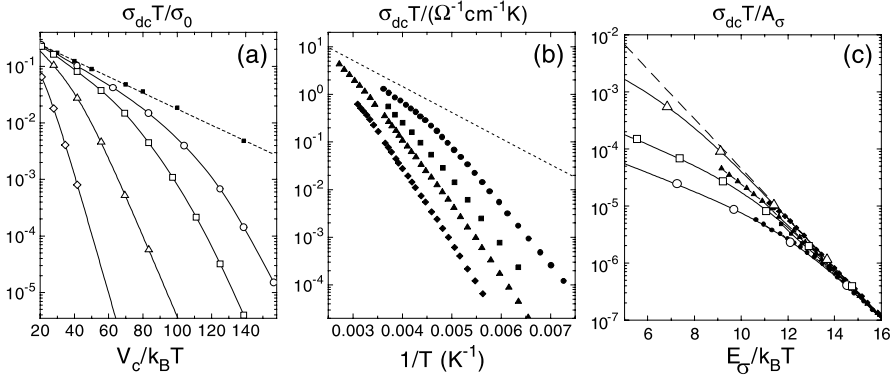**Fig. 20.10.** Arrhenius plots of the dc conductivity $\sigma_{\mathrm{dc}}T$ (a) in model II, cf. (20.18) in units of $\sigma_0$ for $\sigma_\epsilon/V_c = 0$ (■), 0.0115 (○), 0.018 (□), 0.036 (△), and 0.072 (◇), and (b) for $z\mathrm{AgI}+(1-z)[0.525\mathrm{Ag_2S}+0.475(\mathrm{B_2S_3{:}SiS_2})]$ in units of $\Omega^{-1}\mathrm{cm}^{-1}\mathrm{K}$ for $z = 0$ (◆), 0.2 (▲), 0.3 (■), and 0.4 (●) (redrawn from [20]). The dashed lines indicate the upper mobility limit predicted by the model. In (c) the data from (a) and (b) are shown together as functions of $E_\sigma/k_\mathrm{B}T$ and are normalized with respect to the preexponential factors $A_\sigma$ in the corresponding Arrhenius laws. The solid lines in (a) and (c) are drawn as guide for the eye.

and $E_\sigma$ decreases with decreasing $\sigma_\epsilon$. The Arrhenius law is valid up to a crossover temperature $T_x$, where the curves bend toward lower diffusivities. In all cases, the crossover temperature $T_x$ is of the order of $\sigma_\epsilon/k_\mathrm{B}$. For comparison we have redrawn in Fig. 20.10 (b) the experimental conductivity data [20] for $z\mathrm{AgI}+(1-z)[0.525\mathrm{Ag_2S}+0.475(\mathrm{B_2S_3{:}SiS_2})]$ with mole fractions $z$ between zero and 0.4. Evidently, when increasing $z$, the experimental behavior is analogous to the model behavior when decreasing $\sigma_\epsilon$: $E_\sigma$ becomes smaller and the non-Arrhenius behavior starts to occur at lower $T$.

The similarity between the results found in the model and in the experiment becomes even more evident in Fig. 20.10 (c), where the data from Fig. 20.10 (a) and Fig. 20.10 (b) are plotted in the same way as in Fig. 20.9 (b). The experimental curve for $z = 0.4$ is almost perfectly reproduced by the model when $\sigma_\epsilon = 0.0115V_c$ (see the filled and open circles in Fig. 20.10 (c)). The experimental curves for $z = 0$, 0.2 and 0.3 correspond to disorder strengths within a range $0.015V_c < \sigma_\epsilon < 0.036V_c$. It is remarkable that the model not only gives a good fit to the overall shape of the conductivity curves but also reproduces the small values of $k_\mathrm{B}T_x/E_\sigma$. Within the framework of the model, the non-Arrhenius behaviour thus may be explained as a cross-over from a high activation energy at low temperatures, where the ionic motion is dominated by disorder and interaction effects, to a low activation energy at high temperatures, where only the interaction is relevant.

## 20.6 Counterion Model and the "Nearly Constant Dielectric Loss" Response

Models with smooth distribution of uncorrelated site energies, as implied by (20.18), have been studied also with respect to ac transport properties [39], in addition to dc transport considered in the foregoing section. Generally speaking, the outcome for time-dependent mean square displacements and frequency-dependent conductivities in Coulomb lattice gases with Gaussian and percolative disorder (Sect. 20.4) is similar, provided $\Gamma \gg 1$. Qualitative features of conductivity spectra are therefore robust with respect to the particular type of disorder, an issue which is important for understanding their "universal" nature [26].

Let us turn now to yet another disorder model, the counterion model (20.19), which will allow us to discuss both composition-dependent dc-transport properties and dispersive effects, including "nearly constant loss" (NCL)-type high-frequency phenomena [40].

Clearly, in that model with $c \ll 1$ two nearby counterions are separated by a Coulomb barrier whose height is a sensitive function of their distance $2r_s$. Consequently, we observe Arrhenius behavior for both $\sigma_{dc}$ and $\tau_\sigma$ with an activation energy $E_\sigma(c)$ determined by that Coulomb barrier, which grows with decreasing concentration $c$. From simulations one can extract $E_\sigma(c) \simeq$ const $- 0.11(e^2/a) \ln c$ in the relevant concentration range, a variation with $c$ on an energy scale of order 1 electronvolt, which favourably compares with some experiments, see also Sect. 20.7. Regarding dc transport, other notable features of the counterion model are preexponential factors in the Arrhenius law for $\sigma_{dc}$ satisfying the Meyer-Neldel compensation rule [60] and Haven ratios (see Sect. 20.2) which decrease sharply with increasing $c$ for dilute systems, in qualitative accord with the measurements [61].

The dynamic conductivity in the counterion model with $c \ll 1$ displays four distinct frequency regimes and reflects the experimental behavior of dilute samples in a wide frequency range. Those regimes can directly be connected with specific kinds of ionic motions in space and time [62]. Figure 20.11 shows a typical set of data for $\sigma'(\omega)$, normalized by the high-frequency conductivity $\sigma(\infty)$. Below the usual high-frequency plateau (regime I, defined by $\omega > \tau_{MC}^{-1}$, where $\tau_{MC}$ is one Monte Carlo time step) a second regime II appears where $\sigma'(\omega)$ raises with $\omega$ approximately in a linear fashion. This effect will be discussed below in greater detail. A simultaneous analysis of the mean square displacement shows that regime II has limits $\tau_1^{-1} < \omega < \tau_{MC}^{-1}$, where $\tau_1$ is defined by $\langle r^2(\tau_1) \rangle = a^2$. Therefore, in II, the ions essentially remain bound to a counterion and are able to perform only local motions of the character of dipolar reorientation steps. Regime III, related to the Jonscher regime, corresponds to escape processes out of the Coulomb trap. This interpretation is confirmed by noting that the conductivity relaxation time $\tau_\sigma$ in this model satisfies $\langle r^2(\tau_\sigma) \rangle = r_s^2$, where $r_s = a(3/4\pi c)^{1/2}$ amounts to half the distance between two counterions. Finally, for even lower frequencies
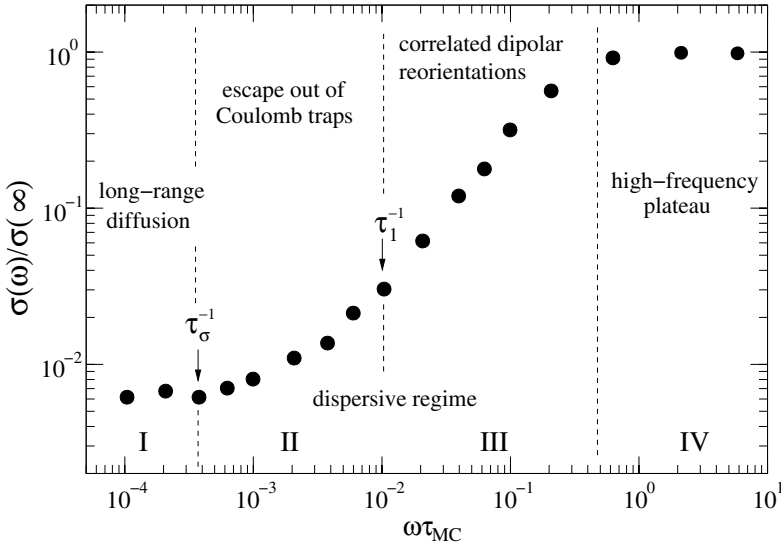
**Fig. 20.11.** Frequency dependence of the conductivity (in a double-logarithmic plot) in the counterion model for $c = 0.03$ and $e^2/ak_BT = 20$. $\tau_{MC}$ corresponds to one Monte Carlo time step (after [40]).

(regime IV, $\omega < \tau_\sigma^{-1}$) the ions can complete effective hops to the next or to further distant counterions, and $\sigma(\omega)$ approaches the dc-plateau.

Now we return to the regime II, where $\sigma'(\omega) \propto \omega$. As mentioned in the introduction (Sect. 20.1), such a behavior in fact is widely observed in glassy materials and defective crystals. The "universal dielectric response" represented by (20.1) therefore has to be supplemented by a high-frequency contribution, see (20.3)

$$\sigma_{NCL}(\omega) \simeq A(T)\omega; \quad \omega > \omega_{NCL}(T) \gg \tau_\sigma^{-1} \tag{20.28}$$

In view of the relationship $\hat{\chi}(\omega) = -4\pi i\hat{\sigma}(\omega)/\omega$ between $\hat{\sigma}(\omega)$ and the dielectric susceptibility $\hat{\chi}(\omega)$, this amounts to a frequency-independent dielectric loss, $\chi''(\omega) \propto A(T)$, known as NCL response. In distinction to the parameters in (20.2), both $A(T)$ and $\omega_{NCL}(T)$ are not thermally activated, but only weakly decrease with temperature [17,63]. Therefore, cooling to helium temperatures, $\sigma_{dc} \propto \tau_\sigma^{-1}$ becomes unmeasurably small while the NCL response (20.28) dominates and typically extends over several orders of magnitude in frequency.

Up to now, the physical origin of the NCL response is unclear. A common picture adheres to the "asymmetric double well potential (ADWP)" model, which rests on the assumption of thermally activated local relaxational steps of charged defects subject to a broad distribution of activation barriers [64].
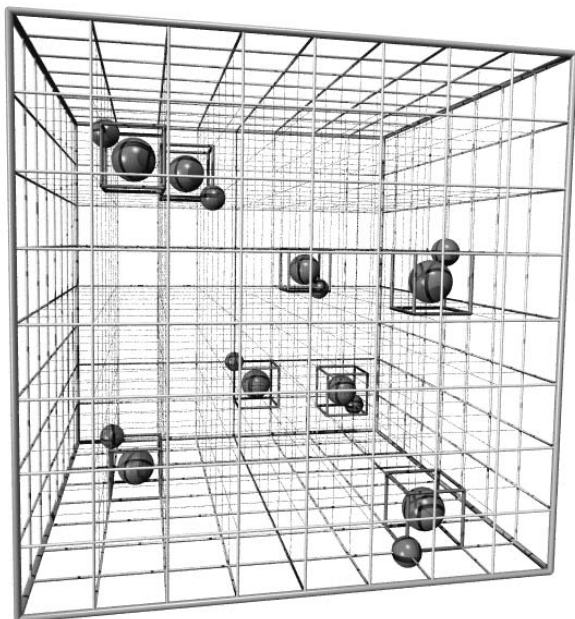
**Fig. 20.12.** Section of the dipolar lattice gas model (after [66]).

Recently, the idea has been advanced that long-range interactions among dipolar centres can give rise to long-time tails in dielectric relaxation, consistent with NCL-type spectra [65, 66]. Evidence for the relevance of this mechanism arose from dynamic Monte Carlo simulations of a "dipolar lattice gas". This model consists of a spatially random assembly of dipolar centres, where charged particles (ions) perform reorientational steps next to their associated immobile counterion. Contrary to the ADWP-model, this model requires no extrinsic local disorder within the individual centres, but emphasises the importance of dipole-dipole interactions.

Clearly, that dipolar lattice gas directly emerges from the counterion model (see Sect. 20.3, (20.19)) and Fig. 20.11, simply by cutting the bonds which leave the first shell surrounding a counterion. Moreover, it is required that each such shell contains exactly one mobile charge carrier. For an illustration see Fig. 20.12. The reduced number of configurations in comparison with the full counterion model clearly facilitates numerical simulations and also allows us to set up analytic approaches, namely exact diagonalization of the underlying master equation for small systems and a dynamic pair approx-
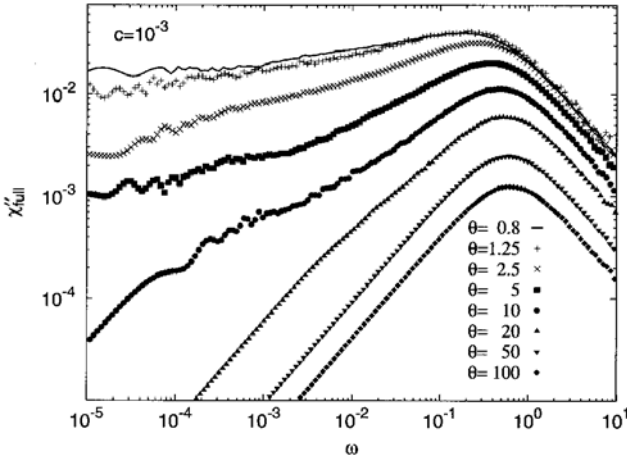
**Fig. 20.13.** Dielectric loss spectrum $\chi''(\omega)$ of a dipolar lattice gas with $c = 10^{-3}$ at different reduced temperatures $\theta = k_B T/V_{\mathrm{dip-dip}}$, showing the gradual transition between Debye and NCL behavior (for a specification of parameters see [66]).

imation [67,68]. For details we refer to the original works. In Fig. 20.13 we present a set of simulated loss spectra for a fairly dilute system with a fraction $c = 10^{-3}$ of dipolar centers relative to the total number of unit lattice cells. Temperature enters via the ratio $\theta = k_B T/V_{\mathrm{dip-dip}}$, where $V_{\mathrm{dip-dip}}$ denotes the typical interaction strength between centers. Rather than simulating the current correlation function, it is more convenient in this case to obtain the correlation function of the total polarisation $\boldsymbol{P}(t) = \sum \boldsymbol{p}_i(t)$, which is a sum over the dipole moments of all centers, and to use

$$\chi''(\omega) = \frac{\beta\omega}{3}\mathrm{Re}\int_0^\infty \langle \boldsymbol{P}(t) \cdot \boldsymbol{P}(0)\rangle e^{i\omega t}\,dt \tag{20.29}$$

Similar to Sect. 20.4 it turns out that the qualitative behavior of $\chi''(\omega)$ is already contained in the "self-part" $\chi''_{\mathrm{self}}(\omega)$ being determined by the self-correlation function $\langle \boldsymbol{p}_i(t)\boldsymbol{p}_i(0)\rangle$. This quantity can be decomposed into a short-time contribution, which corresponds to relaxation of a selected dipole in a static energy landscape due to the other dipoles and a long-time contribution due to temporal renewals in the minimum energy position of that individual dipole. The latter process turns out to be responsible for the slow decay at long times and for NCL behavior, in contrast to the Debye-like behavior of the initial decay [26].

Further notable features of this model are a significant enhancement of the overall NCL response $\chi''(\omega)$ relative to the "self-part" $\chi''_{\mathrm{self}}(\omega)$, the appearance of different concentration-dependent scenarios in approaching a constant loss under decreasing temperature and a robustness of the results against changes in the character of positional disorder [66].

## 20.7 Compositional Anomalies

In ion-conducting glasses long-range transport properties depend in an un-expected anomalous way on the composition of mobile ions. One anomaly refers to the dependence of the conductivity on the ionic concentration. Experiments show that the dc conductivity $\sigma_{\mathrm{dc}}$ raises very steeply with the ion content [69]. Taking $Na_2O$-$B_2O_3$ glasses at 300°C as an example, the conductivity increases approximately by a factor $10^6$ as the mole fraction of $Na_2O$ is increased from 0.15 to 0.5. As mentioned in Sect. 20.6, the variation of the conductivity can in general be described by an activation energy that decreases logarithmically with the ionic concentration $c$, $E_\sigma \simeq A - B\ln(c)$. This behavior corresponds to a power law dependence $\sigma_{\mathrm{dc}} \sim c^{B/k_{\mathrm{B}}T}$, where the exponent $B/k_{\mathrm{B}}T$ becomes much larger than one at low $T$.

Another anomaly pertains to the variation of the conductivity if one type of mobile ion A is successively replaced by a another type of mobile ion B. As a function of the mixing ratio $x = c_{\mathrm{B}}/(c_{\mathrm{A}} + c_{\mathrm{B}})$, where $c_{\mathrm{A}} = (1-x)c$ and $c_{\mathrm{B}} = xc$ are the partial concentrations ($c = c_{\mathrm{A}} + c_{\mathrm{B}}$), $\sigma_{\mathrm{dc}}(x)$ runs through a minimum that becomes more pronounced with decreasing temperature. Well below the calorimetric glass transition temperature $T_g$, the conductivity at the minimum is several orders of magnitude lower than the conductivities of the corresponding single ionic glasses ($x = 0, 1$). For example, in $x$K$_2$O$(1-x)$Li$_2$O·2SiO$_2$ glasses at 150°C, the minimum conductivity is about $10^4$ times smaller than that of either single cation glass. In fact, all properties of glasses that are strongly affected by long-range motions of mobile ions (tracer diffusion coefficients, conductivity, internal friction, viscosity, etc.), show strong deviations from a simple additive behavior upon mixing of two different types of mobile ions. This phenomenon is known as the mixed alkali effect [70] and occurs in all ionically conducting glasses, regardless of the types of ions that are mixed and the type of network constituents forming the disordered host matrix for the ionic motion. Of fundamental importance for the effect are the behaviors of the tracer diffusion coefficients $D_{\mathrm{A}}$ and $D_{\mathrm{B}}$ of ion species A and B. When A ions are replaced by B ions, $D_{\mathrm{A}}$ always decreases and $D_{\mathrm{B}}$ always increases (and vice versa). These changes in the diffusivities are caused by changes in the respective activation energies $E_{\mathrm{A,B}}$, such that $D_{\mathrm{A}}$ and $D_{\mathrm{B}}$ vary by several orders of magnitude at low temperatures $T$.

Like the dispersive transport properties, these compositional anomalies can be understood from lattice gas models with fluctuating site energies. As discussed in Sect. 20.5, the activation energy $E_\sigma$ can, in the presence of a continuous distribution of site energies, be calculated from a critical percolation path argument. Accordingly, $E_\sigma(c) = \epsilon_{\mathrm{c}} - \epsilon_{\mathrm{f}}(c)$ is the difference between the critical energy $\epsilon_{\mathrm{c}}$ determined by the percolation threshold $p_{\mathrm{c}}$ and the Fermi energy $\epsilon_{\mathrm{f}}(c)$ that, due to the filling up of low-energy sites, increases with $c$. A calculation of this $c$-dependence [33, 71] for the Gaussian site energy model (20.18) yields, at intermediate concentrations $c$, a behavior very similar to a logarithmic increase of $\epsilon_{\mathrm{f}}(c)$ with $c$. Accordingly, an approximate logarith-
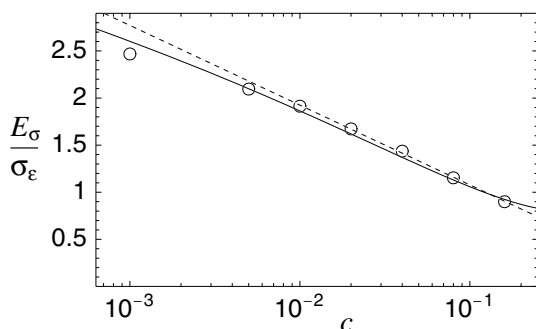
**Fig. 20.14.** Plot of the activation energy $E_\sigma/\sigma_\varepsilon$ as a function of the ionic concentration $c$ in a lattice gas with Gaussian distributed site energies (20.18). The open circles represent the values obtained from Monte Carlo simulations, while the solid line marks the result from the critical path analysis. The dashed lined is a fit with respect to a logarithmic dependence of $E_\sigma$ on $c$, $E_\sigma = A - B\ln(c)$ with $A \cong 0.23$ and $B \cong 0.37$ (redrawn from [71]).

mic decrease of $E_\sigma(c)$ is found, in qualitative agreement with experiment, see Fig. 20.14. For an exponential distribution of site energies, the logarithmic decrease $E_\sigma(c) = A - B\ln c$ comes out exactly [72,73]. It is important to note that the logarithmic behavior can prevail when the Coulomb interactions between the mobile ions are taken into account also [72]. As first shown in [30], the activation energy $E_\sigma(c)$ for the Coulomb lattice gas with uncorrelated site energy disorder can be expressed as a sum of the "structural contribution" $E_\sigma^{(0)}(c) = A - B\ln c$ coming from the critical percolation path analysis and a Coulomb contribution $E_\sigma^{\text{coul}} \propto q^2/r_s \propto q^2 c^{1/3}$. For low concentrations $c$, the behavior is dominated by the structural contribution. Moreover, the logarithmic behavior can be supported by the Coulomb trapping effect of the counterions discussed in Sect. 20.6.

In order to understand the mixed alkali effect one has to realize that different types of ions exhibit distinct local environments in the glassy network. This has been shown by EXAFS measurements [74] and been verified also by means of neutron and X-ray diffraction measurements on mixed alkali phosphate glasses in combination with reverse Monte-Carlo simulations [75]. Accordingly, the energy landscapes $\epsilon_i^A$ and $\epsilon_i^B$ encountered by A and B ions, respectively, must be different; a preferable low-energy site for an A ion is not a preferable low-energy site for a B ion and vice versa. These experimental findings are the starting point of the "dynamic structure model" [76,77]. The central idea of the dynamic structure model is that sites are created in response to the needs of the cations. Thus, in single and in mixed $Na^+/K^+$ ion glass, Na sites are created for $Na^+$ ions and K sites for $K^+$ ions. Structure building in the molten or solid glass depends on the dynamic responses of the network to the moving ions. The preferred sites are created mostly during the cooling process (and possibly, although it is the subject of debate, in

the glass) by an accommodation of the network in the local environment of each mobile ion. Thereby preferred diffusion paths for each type of ion are formed. The dependence of the connectivity of these diffusion paths on the ionic composition was shown to provide an explanation for both the mixed alkali effect and the steep increase of the conductivity with ionic concentration in single modified glasses. For a further discussion of the mixed alkali effect and further developments of the dynamic structure model, which take into account cation size effects and interactions between interchange and network structure, we refer to [78–80]. Signatures of the mixed alkali effect were also found in molecular dynamics studies [37, 81].

Within our description of ionic transport in terms of lattice gases with fluctuating site energies, the simplest approach is to assume that the two ion species move independently of each other and that the sets of low-energy sites for A and B ions are disjoint. Under these assumptions the activation energies $E_A(x)$ and $E_B(x)$ for the tracer diffusion coefficients can be calculated from the activation energies $E_A^{(0)}(c_A)$ and $E_B^{(0)}(c_B)$ of the corresponding single ionic glasses by taking $E_A(x) = E_A^{(0)}((1-x)c)$ and $E_B(x) = E_A^{(0)}(xc)$ [72,73]. Hence, with increasing replacement of A ions by B ions, i.e. increasing $x$, $E_A(x)$ becomes larger while $E_B(x)$ is lowered. As a consequence, $D_A$ decreases and $D_B$ increases very strongly with $x$ at low temperatures.

Comparison with experimental data, however, reveals that this picture of independent ion species is not sufficient. While the *direction* of changes in the activation energies is in qualitative agreement with the experimental data, the dependence of $dE_A(x)/dx$ and $dE_B(x)/dx$ on $x$ is not correctly reproduced. In linear-log plots of the mixing ratio versus the tracer diffusion coefficients, this leads to "curvatures" $\partial^2 \ln D_A/\partial x^2$ and $\partial^2 \ln D_B/\partial x^2$ having wrong signs in comparison with those found in measurements. As shown in Fig. 20.15, however, this problem may be resolved by taking into account the Coulomb interaction between the mobile ions. The Coulomb interaction seems to be of particular importance in the "dilute foreign alkali regimes" $x \to 0$ or $x \to 1$. Since the minority ions in these regimes are immobile on the diffusive time scale of the majority ions, they can, due to the Coulomb repulsion, create "blocking regions" for the majority ions on length scale large compared to the typical jump distance. Immobile minority ions replacing the majority ions in these dilute regimes are thus very effective in interfering the preferred diffusion paths of the majority species and lead to a very strong reduction of their mobility. The model of ions moving in energy landscapes being different for different types of ions allows one to address further important issues [72]: (i) the degree of validity of the empirical Meyer-Neldel rule (cf. Sect. 20.6), (ii) the mixed alkali internal friction peaks occurring in mechanical relaxation spectra, (iii) the behavior of a third tracer impurity ion in a binary mixed alkali glass as measured in [82], and (iv) the question if a clustering of like ions should be expected.
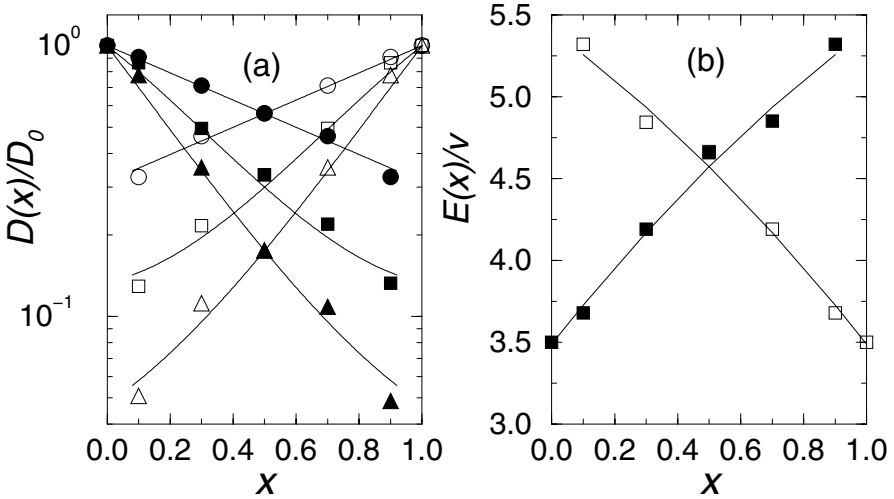
**Fig. 20.15.** (a) Monte-Carlo results for normalised tracer diffusion coefficients $D_{A,B}(x)$ of two ion types A and B as a function of their mixing ratio $x = c_B/(c_A + c_B)$ in a lattice gas with exponentially distributed and uncorrelated site energies $\epsilon_i^A$ and $\epsilon_i^B$ (redrawn from [72]). Long-range Coulomb interactions between the mobile ions were taken into account in the simulations. Full symbols refer to ion type A, open symbols to ion type B, and different symbol types refer to different temperatures. The activation energies $E_{A,B}(x)$ are shown in (b). For a specification of the parameters, see [72].

Before closing this section, we note that a mixed alkali effect also occurs in certain crystals with structure of $\beta$- and $\beta''$-alumina type, where the ionic motion is confined to two-dimensional conduction planes [83–87]. For this effect a quantitative theoretical description is possible [88, 89] due to a wealth of structural information (see e.g. [85, 90, 91]). This theory is based on the fact that A and B ions have a different preference to become part of mobile defects, and this preference is caused by a different interaction of the ions with the local environment. Hence, the very origin of the mixed alkali effect in crystals and glasses might be similar. On the other hand, since the concentration of mobile ions in the crystals is large and since there is no strong structural disorder in the conduction planes, Fermi- and critical energies are not relevant. Instead, blocking and redistribution effects of ions in the conduction planes are important to understand the mixed alkali effect in the crystalline systems (see [88, 89] for a detailed discussion of these points).

## 20.8 Ion-Conducting Polymers

In the preceding sections we discussed charge transport in lattice gases that exhibit frozen disorder either by introducing at random a certain fraction of inaccessible sites (percolative disorder) or through some randomness in the site energies. The assumption of ion diffusion in a rigid matrix showing structural randomness on interatomic length scales turned out to constitute a general frame for the description of ionic transport in inorganic glasses and highly defective crystals.

As indicated already in the introduction (Sect. 20.1), a significantly more complex situation occurs in ion-conducting polymers [23,92]. Prototype materials are polymer-salt solutions based on polyethylene-oxide (PEO). The electronegative oxygen atom in the repeat unit of the PEO-chain tends to bind cations and hence favors salt dissociation. Above their glass transition temperature such systems can exhibit significant ionic conductivities. Distinctive features in comparison with inorganic glasses are the simultaneous diffusion of cations and anions and, most important, matrix fluctuations through the polymer segmental motions, which stochastically provide pathways for ion migration. This last issue is important also in problems of gas permeation through polymer membranes [93], but coupling of the diffusing particles with network degrees of freedom is much stronger in the polymer electrolytes discussed here.

Detailed insight into the coordination of cations by polymer chain segments and the resulting migration mechanisms emerged during recent years from classical molecular dynamics simulations, mostly on alkali-halide/PEO-systems [94–97]. Moreover, for understanding general trends in the ion and chain diffusion properties under varying temperature, pressure and salt-content, a coarse-grained description in terms of stochastic lattice models has proved useful [98–100]. Below we briefly outline this kind of approach. Subsequently we turn to a simplified, athermal model for particle diffusion in a fluctuating network of chain molecules. A mapping of that model onto dynamic percolation theory is proposed [101, 102]. Favorable tests against Monte Carlo simulations suggest that dynamic percolation could become a useful concept for studies of diffusion in fluctuating realistic structures. Finally, we adopt a more macroscopic viewpoint and summarize some ideas, based on differential effective-medium theory [103], how to interpret the recently discovered enhancement of ionic conductivities in stretched polymer systems [104].

### 20.8.1 Lattice Model of Polymer Electrolytes

For PEO-type electrolytes we adopt a simple model of lattice chains, where beads occupy a sequence of nearest-neighbour points on a simple cubic lattice of spacing $a$. We distinguish between C-beads and X-beads in sequences $C(XCC)_n$, where X corresponds to an oxygen atom and C to a hydrocarbon
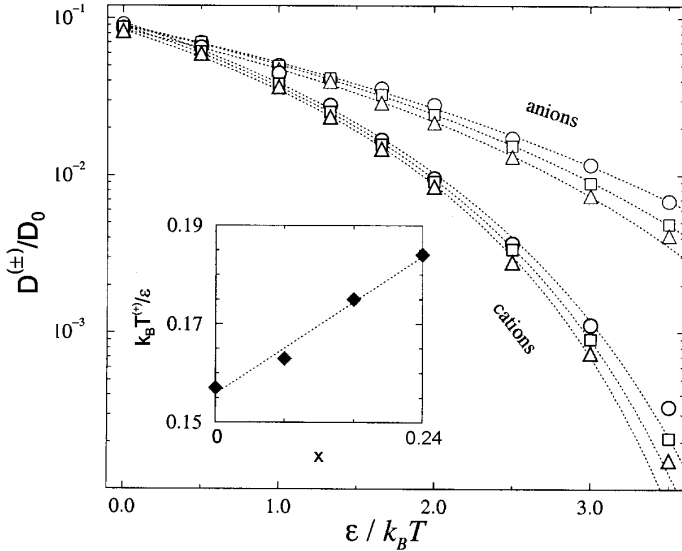
**Fig. 20.16.** Temperature-dependent cation and anion diffusion coefficients $D^{(\pm)}$ (normalized by the diffusion coefficient $D_0$ of non-interacting point particle) versus inverse temperature (data points) and VFT-fits (dotted lines) for different ion concentrations $x = 0.08$ (circles), $x = 0.16$ (squares) and $x = 0.24$ (triangles). The inset shows the variation of the VFT-temperature $T^{(+)}(x)$ with $x$ (after [100]).

group. The total length of the chain is $r = 3n + 1$. Beads on nearest neighbor positions interact with a common repulsion $\epsilon_0 > 0$, which drives the system from the fluid to a glassy state upon lowering the temperature. Ions are represented as point particles carrying charges $\pm q$, and experience their mutual Coulomb forces. The asymmetry in the cation-chain and anion-chain interactions is introduced by assuming that $X$-beads attract cations with strength $-\epsilon < 0$. In order to reduce the number of free parameters in our model, we assume that $\epsilon_0 = \epsilon$. Elementary moves of the chains follow the generalized Verdier-Stockmayer algorithm [105,106], including kink jump, end jump and crankshaft moves. Such moves are known to conform with Rouse-dynamics in the case of sufficiently long chains (see Chap. 13). Ions simply perform nearest-neighbor hops. Transition probabilities in our Monte Carlo simulations are given by the Metropolis algorithm. For further details we refer to the original literature [100]. Considering techniques of lattice Monte Carlo simulations for polymers, we should remark at this point that the dynamics of dense polymer melts, especially their associated scaling properties, are most efficiently investigated by using the bond-fluctuation model [107]. However, in view of the chemical heterogeneity within a repeat unit in PEO-chains and the specific interactions of ions with chain beads it seems more natural in the present context to employ the lattice chain model described above.

Now we turn to some representative results. Figure 20.16 shows Arrhenius plots of the diffusion coefficients $D^{(\pm)}$ and $D^{(P)}$ for cations, anions and the polymer center of mass, respectively. The downward curvature of the data allows fits in terms of the empirical Vogel-Fulcher-Tammann (VFT) equation, well-known from relaxation studies in supercooled fluids [24],

$$D^{(\alpha)}(T, x) = D_\infty(x) \exp\left(-\frac{E^\alpha(x)}{k_{\rm B}(T - T^{(\alpha)}(x))}\right) \qquad (20.30)$$

where $\alpha = \pm, P$. The ion concentration enters through the parameter $x$ which measures the number of cations relative to the number of $X$-beads in the sample. $E^\alpha(x)$ is a characteristic energy and $T^{(\alpha)}(x)$ the VFT-temperature. For low ion content, $x \ll 1$, one finds that $T^+(x) \simeq T^{(P)}(x)$, which confirms the strong coupling of cations to the chain beads and suggests that freezing of the network simultaneously suppresses cation diffusion. By contrast, anion diffusion shows a much weaker temperature dependence, with $T^{(-)}(x) < T^{(P)}(x)$. VFT-temperatures generally increase with $x$, as indicated in the inset of the figure. These findings agree qualitatively with diffusion measurements on PEO-based electrolytes by the NMR pulsed-field gradient method [108], cf. Chap. 10, and with the general experimental observation of an increase in the glass transition temperature $T_g$ with $x$ [109].

The VFT-expressions (20.30) together with the equality $T^{(+)}(x) \simeq T^{(P)}(x)$ for $x \ll 1$ immediately imply, for fixed $x$, that

$$D^{(+)}(T, x) \propto (D^{(P)}(T, x))^{n_+(x)} \qquad (20.31)$$

where the exponent

$$n_+(x) = E^{(+)}(x)/E^{(P)}(x) \quad < 1 \qquad (20.32)$$

decreases with increasing $x$. Thus, when temperature is varied, the cation diffusion coefficient depends in a power-law fashion on the diffusion coefficient for the chain center-of-mass motion. As shown in Fig. 20.17, such a relationship holds over at least three decades in $D^{(+)}$. Qualitatively, we expect that diffusion coefficients of non-entangled chains reflect the behavior of the viscosity $\eta$ of the system, $D^{(P)} \sim \eta^{-1}$. Equation (20.31) would then imply $D^{(+)} \sim \eta^{-n_+}$. Such a relationship appears interesting in connection with recent experimental observations of a "fractional Stokes-Einstein" law in ionic melts [110]. Figure 20.17 also shows that under variation of both $T$ and $x$ the anion diffusion coefficients can be represented by a unique function of $D^{(P)}$. This suggests that, for given $T$ and $x$, anion diffusion depends only on a single time scale that characterizes the chain motion, a result which perfectly agrees with the idea of dynamic percolation. There one considers a random walk in an environment with percolative disorder. As time proceeds, the disorder configurations are continually renewed at a certain rate. In Sect. 20.8.2 we shall come back to this model in greater detail.
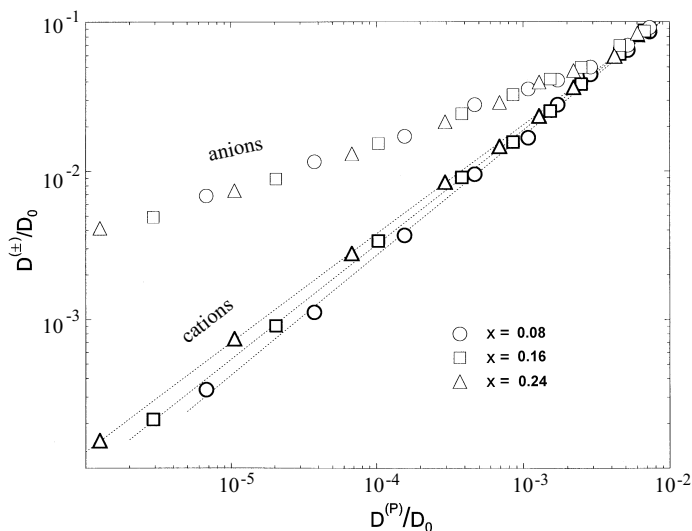
**Fig. 20.17.** Self-diffusion coefficients $D^{(\pm)}$ of cations and anions (normalized by the diffusion coefficient $D_0$ of non-interacting point particle) against chain diffusion coefficients $D^{(P)}$, for different ion concentrations (after [100]).

Several further studies have been carried out in a reduced polymer electrolyte model with only one species of mobile point-like particles. The latter assumption may directly apply to the so-called ionenes, where the anions are chemically grafted to the chains [111]. By combining the quasi-chemical approximation for the equation of state with standard simulations at constant volume, information on the isobaric-isothermal ensemble can be gained [112]. Ion diffusion coefficients in dense systems were found to decrease exponentially with pressure, in accord with experiments [111]. Further studies considered the variation of VFT-temperatures with salt concentration, keeping the pressure fixed. As $x$ becomes of the order of unity, the VFT-temperatures $T^+(x)$ and $T^{(P)}(x)$ tend to saturate in this model and get decoupled, $T^+(x) < T^{(P)}(x)$, such that ions keep some mobility when the network freezes.

## 20.8.2 Diffusion through a Polymer Network: Dynamic Percolation Approach

With the aim to investigate generic aspects of random walks in a dynamically disordered environment, several authors have developed models of dynamic percolation (DP) [113–116]. The most common starting point is a bond percolation model with global, instantaneous renewals of the disorder configurations. These renewal events occur in time according to some waiting time distribution $\psi(t)$. Denoting by $\langle r^2(t) \rangle_0$ the mean square displacement of the

walker in the absence of renewals (frozen disorder), one can show [117] that the long-time (zero-frequency) diffusion coefficient in $d = 3$ dimensions is given by

$$D = \frac{1}{6} \frac{\int_0^\infty dt \, \psi(t) \langle r^2(t) \rangle_0}{\int_0^\infty dt \, \psi(t) t} \tag{20.33}$$

In the special case of a Poisson renewal process with mean waiting time $\lambda^{-1}$, we have $\psi(t) = \lambda^{-1} e^{-\lambda t}$, so that $D = D_0(\lambda)$, where $D_0(\lambda)$ is determined by the Laplace transform of $\langle r^2(t) \rangle_0$. More generally, the frequency-dependent diffusivity $D(-i\omega)$ in the case of Poisson renewals satisfies the analytic continuation rule [113]

$$D(-i\omega) = D_0(-i\omega + \lambda) \tag{20.34}$$

In an attempt to map a random walk through a system of fluctuating polymer chains onto that model, the primary task is to extract an appropriate waiting time distribution $\psi(t)$, to be used in (20.33), from the actual polymer dynamics. For that purpose the following scheme has been advanced recently [102,118]. The function $\psi(t)$ is related to the stochastic process $n_i(t)$, representing the occupation of a site $i$ by a polymer bead. That site $i$ is chosen to be a nearest neighbor of a fixed position of the walker. By this, the correlation function $\langle n_i(t) n_i(0) \rangle$ reflects the closing or opening statistics of a bond connected to the walker. Renewal events in an associated DP model are now identified with occupational changes at site $i$. This will allow us to express $\psi(t)$ in terms of $\langle n_i(t) n_i(0) \rangle$.

To put this idea on a quantitative basis, we introduce the probability $\Phi(t)$ with $t > 0$ that no renewal takes place in the interval $[0, t]$, after a previous renewal at an arbitrary time $t_0 < 0$. Hence, with probability $\Phi(t)$ the occupation of site $i$ does not change, so that $n_i(t) = n_i(0)$, with possible values 0 and 1, and $n_i(t) n_i(0) = (n_i(0))^2 = n_i(0)$. Conversely, with probability $1 - \Phi(t)$, one or more renewals occur within $[0, t]$. Then, since configurations are randomly reassigned, $n_i(t)$ can be replaced by its average $c$, and $n_i(t) n_i(0) = c \, n_i(0)$. Averaging in addition over the initial occupation $n_i(0)$, we obtain

$$\langle n_i(t) n_i(0) \rangle = c \, \Phi(t) + c^2 (1 - \Phi(t)) \tag{20.35}$$

or

$$\Phi(t) = \frac{\langle n_i(t) n_i(0) \rangle - c^2}{c(1 - c)} \tag{20.36}$$

The final step is to utilize the result from renewal theory [117], that

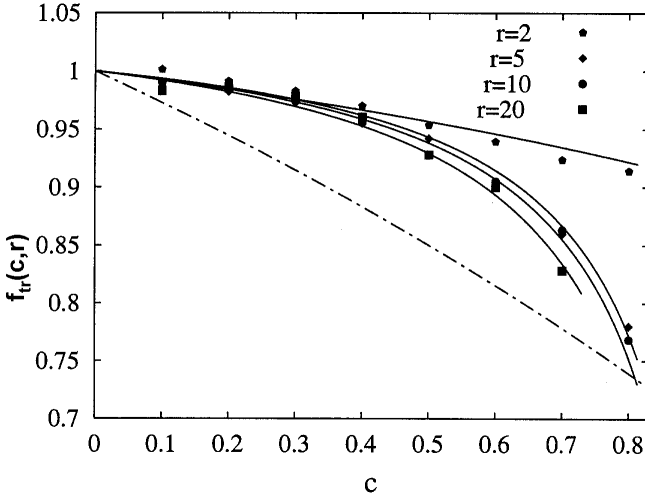$$\psi(t) = \bar{\lambda}^{-1} \Phi''(t) \tag{20.37}$$

**Fig. 20.18.** Comparison of tracer correlation factors from dynamic percolation theory for chains of different lengths $r$ (data points) with results from simulations (full lines, representing fit functions of simulation data). The dashed-dotted line shows the tracer correlation factor of a hard core lattice gas that corresponds to $r = 1$.

where $\bar{\lambda}^{-1} = \int_0^\infty dt\, \psi(t)t$ is the mean renewal time. These arguments generalize earlier ideas of constructing effective-medium theories for many-particle systems with the help of DP theory [119].

When applying this concept, based on (20.33), (20.36) and (20.37), to tracer diffusion within a polymer host, one has to find the two input quantities $\langle r^2(t)\rangle_0$ and $\langle n_i(t)n_i(0)\rangle$ from simulations of the two separate problems: random walk of a tracer particle through a frozen polymer host and local occupational correlation function due to polymer segmental motions next to a frozen tracer. Both of these problems are expected to be computationally much less demanding than the simulation of the full system dynamics.

Recently that DP scheme has been tested against Monte Carlo simulations for the case of an athermal model, where multiple occupation of lattice sites by either chain beads or (point-like) tracer particles is excluded [102]. As usual, we define the tracer correlation factor $f_{\mathrm{tr}}(c, r)$ in terms of the tracer diffusion coefficient $D$ by

$$D = (1 - c)f_{\mathrm{tr}}(c, r)D_0 \qquad (20.38)$$

which now depends both on the overall concentration $c$ of occupied sites and on the chain length $r$. Data points in Fig. 20.18 show DP results for $f_{\mathrm{tr}}(c, r)$ up to a chain length $r = 20$, while the full lines represent fits to Monte Carlo simulations of the complete system dynamics. Obviously the agreement

between both methods is excellent, suggesting that the DP description may become a useful tool also in studies of more realistic systems. It is important to note that in order to achieve this degree of accuracy in DP theory, the non-Poisson character of the waiting-time distribution has to be taken into account. In particular, the function $\Phi(t)$ reflecting the polymer dynamics shows slow relaxation which for longer chains becomes even more pronounced.

Figure 20.18 includes data for the well-known case of a hard core lattice gas, which emerges here as the limit $r = 1$. Since for $c < 0.8$ one finds $f_{tr}(c, 1) < f_{tr}(c, r)$ with $r \neq 1$, we conclude that in this concentration range chain connectivity enhances tracer diffusion. This conforms with the additional observation that a random walker in a $3 - d$ system of frozen chains ceases to percolate at a threshold concentration $c_{crit}(r)$ which increases with $r$.

### 20.8.3 Diffusion in Stretched Polymers

Recent experiments on stretched PEO-based polymer electrolyte films have revealed an enhancement of ionic diffusion and conductivity in the stretch direction, while these transport coefficients in the normal direction decrease [104]. A preferential migration of cations along the helical structure of the PEO-chain, detected in molecular dynamics simulations [94], can in principle lead to that kind of macroscopic anisotropy when chains get oriented through stretch. This situation has been described qualitatively by an effective two-phase model, where a highly conducting phase is associated with those oriented molecular structures, but is surrounded by poorly conducting boundary regions [103]. The effective conductivity was evaluated by using differential effective-medium theory (DEMT), which accounts for the fact that the highly conducting phase with conductivity $\sigma_2$ never percolates; rather, the conduction paths always have to pass the boundary phase with conductivity $\sigma_1 \ll \sigma_2$. Under stretch, the shape of one-phase regions changes from spherical to prolate-ellipsoidal. As a stretch parameter one uses the ratio $\lambda$ between the long and the short axis of these ellipsoids. A version of DEMT capable of taking into account these non-spherical shapes is due to Mendelson et al. [120].

Conductivities perpendicular and parallel to the stretch direction are plotted in Fig. 20.19 as a function of $\lambda$ for different volume fractions $f_2$ of the highly conducting phase. While the directions of change in $\sigma_\parallel$ and $\sigma_\perp$ with $\lambda$ agree with experiments, the model calculations show further details which remain to be tested against more refined measurements. For example, as $f_2$ increases, $\sigma_\parallel(\lambda)$ becomes more sensitive to changes in $\lambda$, whereas $\sigma_\perp$ becomes less sensitive. Clearly, in the interpretation of these and other features of that model, care has to be taken in relating the degree of macroscopic stretch to anisotropies on the molecular level.
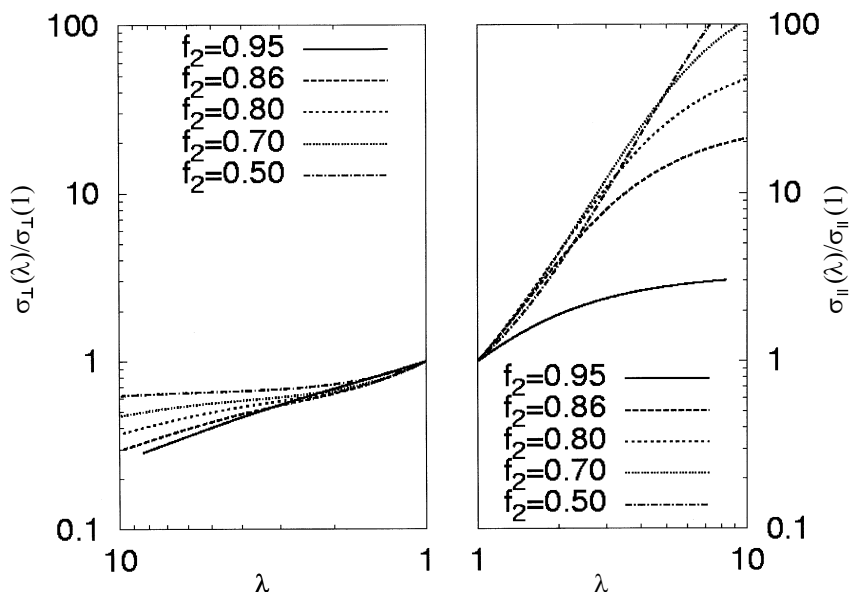
**Fig. 20.19.** Ratio between conductivities of the stretched film in the stretch direction (right) and perpendicular to it (left) and the conductivity in the isotropic unstretched film $(\sigma_\perp(1) = \sigma_\parallel(1))$ as a function of the stretch parameter $\lambda$ for several values of the volume fraction $f_2$ of the low-conductivity phase with $\sigma_1/\sigma_2 = 10^{-4}$ (after [103]).

## 20.9 Conclusion

In Sects. 20.3–20.6, models for ionic transport in complex systems have been presented which keep the essential physics: Coulombic interaction between the ions and structural disorder in the substrate. These models are simple enough to be treated numerically by Monte-Carlo simulation techniques. Several ionic transport quantities, such as the mean square displacement, the frequency dependent conductivity and the spin-lattice relaxation rate, have been discussed and it was found that *both* ingredients (structural disorder *and* Coulomb interactions) are needed to find the typical dispersion behavior widely observed in experiments. It is remarkable that inclusion of the simple percolative type of disorder allows one to account for the delicate differences between conductivity relaxation and spin-lattice relaxation found in experiments. However, for the theoretical understanding of the non-Arrhenius behaviour observed in fast ion conductors the consideration of the different energies associated with the different environments encountered by the mobile ions becomes important.

   In Sects. 20.4 and 20.5 it has been assumed that the charges of the mobile cations are balanced by a homogeneous background charge, and that the en-

ergetic disorder is spatially uncorrelated. On the other hand, the assumption of randomly placed immobile counterions leads to a spatially correlated one-particle energy landscape. Local motions of ions on binding sites next to an associated counterion can give rise to a "nearly constant loss"-type response. This was shown by additional simulations of a dipolar lattice gas discussed in Sect. 20.6. Other effects caused by spatial correlations in the disorder are considered in [121]. By taking into account that the energetic disorder is different for different types of mobile ions, a natural explanation for the mixed alkali effect in glasses was discussed in Sect. 20.7. Coulomb interaction effects are important to understand why the long-range mobility of a particular ion type behaves quite differently if its concentration is changed via dilution or if its (partial) concentration is changed via replacement by another type of mobile ion.

Furthermore we have shown in Sect. 20.8 that a stochastic model of lattice polymers and point-like particles (ions) with specific interactions can account for characteristic conductance and network relaxational properties of polymer electrolytes. On a coarse-grained level, dynamic percolation theory appears as a promising tool to study ionic diffusion through a fluctuating polymer matrix.

## Notation

| | |
|---|---|
| $a, L$ | lattice constant, system size |
| $d$ | space dimension |
| $D, D_{\mathrm{st}}$ | long-time, short-time diffusion coefficient |
| $D(t)$ | time dependent diffusion coefficient |
| $\hat{D}(\omega)$ | complex frequency dependent diffusion coefficient |
| $\Delta E_{\mathrm{SLR}}$ | activation energy of the correlation time in spin-lattice relaxation |
| $E_1^{\mathrm{SLR}}, E_2^{\mathrm{SLR}}$ | activation energy of spin-lattice relaxation rate at high- and low-temperature side of maximum |
| $E_\sigma, \Delta E_f$ | activation energy of conductivity and tracer correlation factor |
| $f_{\mathrm{tr}}$ | tracer correlation factor |
| $G^{(q)}(t)$ | correlation function for spin-lattice relaxation |
| $\hat{H}_{\mathrm{R}}(\omega)$ | complex Haven ratio |
| $I, Q$ | spin and quadrupole moment of nucleus |
| $\boldsymbol{j}(t)$ | current density |
| $\langle \boldsymbol{j}(t) \cdot \boldsymbol{j}(0) \rangle$ | current auto-correlation function |
| $n_\sigma, n_{\mathrm{D}}$ | conductivity and diffusion exponent |
| $p$ | fraction of lattice sites accessible for mobile ions |
| $p_{\mathrm{c}}$ | percolation threshold |
| $P(\boldsymbol{r}, t)$ | diffusion propagator |
| $\boldsymbol{P}(t)$ | electric polarization |
| $r$ | length of polymer chains |
| $\langle r^2(t) \rangle$ | mean square displacement |

| | |
|---|---|
| $\langle r^2(N_{\mathrm{hop}})\rangle$ | mean square displacement as a function of performed hops |
| $S_{\mathrm{inc}}(\boldsymbol{k},\omega)$ | incoherent structure factor |
| $1/T_1(\omega,T)$ | spin-lattice relaxation rate |
| $T_{\max}$ | temperature of maximum in spin-lattice relaxation rate |
| $T^{(\alpha)}$ | Vogel-Fulcher-Tammann temperature for polymer chains ($\alpha = P$), cations ($\alpha = +$) and anions ($\alpha = -$) |
| $V_0$ | structural energy barrier for hops |
| $V_{\mathrm{dip-dip}}$ | dipole-dipole interaction energy |
| $\gamma$ | magnetogyric ratio |
| $\Gamma$ | plasma parameter |
| $\overline{\lambda}$ | mean renewal rate |
| $\nu$ | number of nearest neighbours |
| $\rho$ | number density |
| $\sigma_{||},\ \sigma_{\perp}$ | parallel, perpendicular conductivity in stretched polymer films |
| $\hat{\sigma}(\omega),\ \sigma_{\mathrm{dc}}$ | complex dynamic conductivity, dc-conductivity |
| $\tau_{\infty}$ | rattling time or inverse attempt frequency for hops |
| $\tau_{\mathrm{SLR}}$ | correlation time in spin-lattice relaxation |
| $\tau_{\sigma},\ \tau_{\mathrm{D}}$ | conductivity and diffusion relaxation time |
| $\hat{\chi}(\omega)$ | complex dielectric susceptibility |
| $\psi(t)$ | waiting time distribution for renewals |
| $\psi(\tau_{\mathrm{w}})$ | effective distribution of waiting times $\tau_w$ |
| $\omega_{\mathrm{NCL}}$ | cross-over frequency to "nearly constant loss" regime |

# References

1. H. Jain, N.L. Peterson, H.L. Downing: J. Non-Cryst. Solids **55**, 283 (1983)
2. *Impedance Spectroscopy*, ed by J.R. Macdonald (John Wiley & Sons, New York 1987)
3. K. Funke: Prog. Solid St. Chem. **22**, 111 (1993)
4. C.T. Moynihan, L.P. Boesch, N.L. Laberge: Phys. Chem. Glasses **14**, 122 (1973)
5. M.D. Ingram: Phys. Chem. Glasses **28**, 215 (1987)
6. O. Kanert, J. Steinert, H. Jain, K.L. Ngai: J. Non-Cryst. Solids **131-133**, 1001 (1991); O. Kanert, R. Küchler, K.L. Ngai, H. Jain: Phys. Rev. B **49**, 76 (1994)
7. O. Kanert, R. Küchler, J. Diekhöfer, X. Lu, H. Jain: Phys. Rev. B **49**, 629 (1994)
8. P. Heitjans, W. Faber, A. Schirmer: J. Non-Cryst. Solids **131-133**, 1053 (1991); P. Heitjans: Solid State Ionics **18/19**, 50 (1986)
9. W. Franke, P. Heitjans: Ber. Bunsenges. Phys. Chem. **96**, 1674 (1992)
10. P. Heitjans, S. Indris: J. Phys.: Condens. Matter **15** R1257 (2003)
11. K. Funke, I. Riess: Z. Phys. Chem. Neue Folge **140**, 217 (1984); K. Funke: Z. Phys. Chem. Neue Folge **154**, 251 (1987)
12. T. Suemoto, M. Ishigame: Phys. Rev. B **33**, 2757 (1986)
13. L. Börjesson, L.M. Torrel, W.S. Howells: Phil. Mag. B **59**, 105 (1989); L. Börjesson Phys. Rev. B **36**, 4600 (1987)

14. G. Carini, M. Federico, G. Tripodo: Phil. Mag. B **65**, 153 (1992)
15. D.P. Almond, G.K. Duncan, A.R. West: Solid State Ionics **8**, 159 (1983)
16. A.K. Jonscher: Nature **267**, 673 (1977)
17. A.S. Nowick, B.S. Lim, A.V. Vaysleyb: J. Non-Cryst. Solids **172**–**174**, 1243 (1994)
18. K.L. Ngai: J. Chem. Phys. **110**, 10576 (1999)
19. H. Jain, S. Krishnaswami, O. Kanert: J. Non-Cryst. Solids **307**–**310**, 1017 (2002)
20. J. Kincs, S.W. Martin: Phys. Rev. Lett. **76**, 70 (1996)
21. K.L. Ngai, A.K. Rizos: Phys. Rev. Lett. **76**, 1296 (1996)
22. M.D. Ingram, C. Vincent, A. Wandless: J. Non-Cryst. Solids **53**, 73 (1982)
23. F.M. Gray: *Solid Polymer Electrolytes* (VCH Publishers, New York 1991)
24. H. Vogel: Physik. Zeitschrift **22**, 645 (1921); G.S. Fulcher: J. Am. Ceram. Soc. **8**, 339 (1925); G. Tammann, W. Hesse: Z. anorg. u. allg. Chem. **156**, 245 (1926)
25. N. Bloembergen, E.M. Purcell, R.V. Pound: Phys. Rev. **73**, 679 (1948)
26. W. Dieterich, P. Maass: Chem. Phys. **284**, 439 (2002)
27. A. Bunde, D.K. Chaturvedi, W. Dieterich: Z. Physik B **47**, 209 (1982); A. Bunde, W. Dieterich: Phys. Rev. B **31**, 6012 (1985)
28. P. Maass, J. Petersen, A. Bunde, W. Dieterich, H.E. Roman: Phys. Rev. Lett. **66**, 52 (1991)
29. M. Meyer, P. Maass, A. Bunde: Phys. Rev. Lett. **71**, 573 (1993)
30. P. Maass, M. Meyer, A. Bunde: Phys. Rev. B **51**, 8164 (1995)
31. K.L. Ngai: Comments Solid State Phys. **9**, 127, 141 (1979); K.L. Ngai. In: *Fast Ion Transport in Solids*, ed by P. Vashishta, J.N. Mundy, G.K. Shenoy (North Holland, New York 1979); K.L. Ngai, O. Kanert: Solid State Ionics **53-56**, 936 (1992)
32. S.R. Elliott, A.P. Owens: Phys. Rev. B **44**, 47 (1991)
33. W. Schirmacher, M. Prem, J.-B. Suck, A. Heidemann: Europhys. Lett. **13**, 523 (1990)
34. J.C. Dyre: Phys. Rev. B **48**, 12511 (1993)
35. A. Hunt: J. Phys. C **3**, 7831 (1991); **4**, 5371 (1992); J. Non-Cryst. Solids **160**, 183 (1993)
36. H. Lammert, M. Kunow, A. Heuer: Phys. Rev. Lett. **90**, 215901 (2003)
37. J. Habasaki, Y. Hiwatari: Phys. Rev. B **69**, 144207 (2004)
38. M. Vogel: Phys. Rev. B **70**, 094302 (2004)
39. J. Petersen, W. Dieterich: Phil. Mag. B **65**, 231 (1992)
40. D. Knödler, P. Pendzig, W. Dieterich: Solid State Ionics **86**–**88**, 29 (1996)
41. P. Maass, M. Meyer, A. Bunde, W. Dieterich: Phys. Rev. Lett. **77**, 1528 (1996)
42. R. Kubo, M. Toda, N. Hashitsume: *Statistical Physics II* (Springer-Verlag, Berlin Heidelberg New York 1985)
43. A. Abragam: *The Principles of Nuclear Magnetism* (Clarendon Press, Oxford 1962)
44. D. Wolf: *Spin-Temperature and Nuclear-Spin Relaxation in Matter* (Clarendon Press, Oxford 1979)
45. A. Bunde, S. Havlin. In: *Fractals and Disordered Systems*, 2nd edn, ed by A. Bunde, S. Havlin (Springer, Berlin Heidelberg New York 1996)
46. M.D. Ingram: J. Non-Cryst. Solids **131-133**, 955 (1991)
47. J. Hoshen, R. Kopelman: Phys. Rev. B **14**, 3438 (1976)

48. M.P. Allen, D.J. Tildesley: *Computer Simulation of Liquids* (Clarendon Press, Oxford 1987)
49. C. Cramer, K. Funke, T. Saatkamp: Phil. Mag. B **71**, 701 (1995)
50. G.H. Weiss. In: *Fractals in Science*, ed by A. Bunde, S. Havlin (Springer, Berlin Heidelberg New York 1994)
51. H. Scher, M. Lax: Phys. Rev. B **7**, 4491 (1973)
52. J.W. Haus, K.W. Kehr: Phys. Rep. **150**, 263 (1987)
53. A. Bunde, S. Havlin, H.E. Roman: Phys. Rev. A **42**, 6274 (1990)
54. M. Tatsumisago, C.A. Angell, S.W. Martin: J. Chem. Phys. **97**, 6968 (1992)
55. B. Munro, M. Schrader, P. Heitjans: Ber. Bunsenges. Phys. Chem. **96**, 1718 (1992); W. Franke, P. Heitjans, B. Munro, M. Schrader. In: *Defects in Insulating Materials*, ed by O. Kanert, J.M. Spaeth (World Scientific, Singapore 1993) p 1009
56. R. Winter, K. Siegmund, P. Heitjans: J. Non-Cryst. Solids **212**, 215 (1997)
57. E. Bychkov: Solid State Ionics **136 - 137**, 1111 (2000)
58. V. Ambegoakar, B.I. Halperin, J.S. Langer: Phys. Rev. B **4**, 2612 (1971); B.I. Shklovskii A.L. Efros: Zh. Eksp. Teor. Fiz. **60**, 867 (1971) [Sov. Phys. JETP **33**, 468 (1971)]
59. H. Bässler: Phys. Rev. Lett.**58**, 767 (1987)
60. W. Meyer, H. Neldel: Z. Tech. Phys. **12**, 588 (1937)
61. J.E. Kelly III, J.F. Cordaro, M. Tomozawa: J. Non-Cryst. Solids **41**, 47 (1980)
62. P. Pendzig, W. Dieterich: Solid State Ionics **105**, 209 (1998)
63. C.A. Angell, K.L. Ngai, G.B. McKenna, P.F. McMillan, S.W. Martin: J. Appl. Phys. **88**, 3113 (2000)
64. M. Pollak, G.E. Pike: Phys. Rev. Lett. **28**, 1449 (1972)
65. D. Knödler, P. Pendzig, W. Dieterich: Mat. Res. Soc. Symp. Proc. **369**, 225 (1995)
66. T. Höhr, P. Pendzig, W. Dieterich, P. Maass: Phys. Chem. Chem. Phys. **4**, 3168 (2002)
67. P. Pendzig. PhD thesis, University of Konstanz (1998)
68. P. Pendzig, W. Dieterich: Solid State Ionics **105**, 209 (1998)
69. M.D. Ingram. In: *Materials Science and Technology*, vol 9, ed by J. Zarzycki (VCH Verlagsgesellschaft, Weinheim 1991) p 715
70. D.E. Day: J. Non-Cryst. Solids **21**, 343 (1976)
71. M. Porto, P. Maass, M. Meyer, A. Bunde, W. Dieterich: Phys. Rev. B **61**, 6057 (2000)
72. P. Maass: J. Non-Cryst. Solids **255**, 35 (1999)
73. A. Hunt: J. Non-Cryst. Solids **175**, 129 (1994)
74. G.N. Greaves, S.J. Gurman, C.R.A. Catlow, A.V. Chadwick, S. Houde-Walter, C.M.B. Henderson, B.R. Dobson: Phil. Mag. A **64**, 1059 (1991); S.N. Houde-Walter, J.M. Inman, A.J. Dent, G.N. Greaves: J. Phys. Chem. **97**, 9330 (1993)
75. J. Swenson, A. Matic, C. Karlsson, L. Börjesson, C. Meneghini, W.S. Howells: Phys. Rev. B **63**, 132202 (2001)
76. P. Maass, A. Bunde, M.D. Ingram: Phys. Rev. Lett. **68**, 3064 (1992)
77. A. Bunde, M.D. Ingram, P. Maass: J. Non-Cryst. Solids **172**–**174**, 1222 (1994)
78. M.D. Ingram, J.E. Davidson, A.M. Coats, E.I. Kamitsos, J.A. Kapoutsis: Glass Science and Technology **73**, 89 (2000)
79. P.W.S.K. Bandaranayake, C.T. Imrie, M.D. Ingram: Phys. Chem. Chem. Phys. **4**, 3209 (2002); M.D. Ingram, B. Roling: J. Phys.: Condens. Matter **15**, 1595 (2003)

80. A. Bunde, M.D. Ingram, S. Russ: Phys. Chem. Chem. Phys. **6**, 3663 (2004)
81. J. Habasaki, I. Okada, Y. Hiwatari: J. Non-Cryst. Solids **208**, 181 (1996)
82. H. Jain, N.L. Peterson: J. Am. Ceram. Soc. **66**, 174 (1983)
83. G.V. Chandrashekhar, L.M. Foster: Solid State Commun. **27**, 269 (1978)
84. L.M. Foster, M.P. Anderson, G.V. Chandrashekhar, G. Burns, R.B. Bradford: J. Chem. Phys **75** (1981)
85. J.A. Bruce, M.D. Ingram: Solid State Ionics **9&10**, 717 (1983)
86. T. Tsurumi, G. Singh, P.S. Nicholson: Solid State Ionics **22**, 225 (1987)
87. S. Nariki, S. Ito, K. Uchinokura, T. Uchida, N. Yoneda: Solid State Ionics **36**, 193 (1989)
88. M. Meyer, V. Jaenisch, P. Maass, A. Bunde: Phys. Rev. Lett. **76**, 2338 (1996)
89. M. Meyer, P. Maass, A. Bunde: J. Chem. Phys. **109**, 2316 (1998)
90. J.P. Boilot, G. Collin, Ph. Colomban, R. Comes: Phys. Rev. B **22**, 5912 (1980)
91. J.C. Wang, M. Gaffari, Sang-il Choi: J. Chem. Phys **63**, 772 (1975); J.C. Wang, J.B. Bates, T. Kenda, H. Engstrom, D.F. Pickett, Sang-il-Choi. In: *Fast Ion Transport in Solids*, ed by P. Vashista, J.N. Mundy, G.K. Shenoy (Elsevier, Amsterdam 1979)
92. A. Nitzan, M. Ratner: J. Phys. Chem. **98**, 1765 (1994)
93. A.A. Gusev, S. Arizzi, U.W. Suter: J. Chem. Phys. **99**, 2221 (1993)
94. F. Müller-Plathe, W.F. von Gunsteren: J. Chem. Phys. **103**, 4745 (1995)
95. B. Mos, P. Verkerk, S. Pouget, A. van Zon, G.-J. Bel, S.W. de Leeuw, C.D. Eisenbach: J. Chem. Phys. **113**, 4 (2000)
96. J.J. de Jonge, A. van Zon, S.W. de Leeuw: Solid State Ionics **147**, 349 (2002)
97. O. Borodin, G.D. Smith: J. Phys. Chem. B **107**, 6801 (2003)
98. R. Olender, A. Nitzan: J. Chem. Phys. **100**, 705 (1994); **101**, 2338 (1994)
99. R. Olender, A. Nitzan, D. Knödler, W. Dieterich: J. Chem. Phys. **103**, 6275 (1995)
100. P. Pendzig, W. Dieterich, A. Nitzan: J. Non-Cryst. Solids **235**–**237**, 748 (1998)
101. O. Dürr, W. Dieterich, A. Nitzan: Solid State Ionics **149**, 125 (2002)
102. O. Dürr, T. Volz, W. Dieterich, A. Nitzan: J. Chem. Phys. **117**, 441 (2002)
103. O. Dürr, W. Dieterich, P. Maass, A. Nitzan: J. Phys. Chem. B **106**, 6149 (2002)
104. D. Golodnitsky, E. Peled: Electrochimica Acta **45**, 1431 (2000)
105. P.H. Verdier, W.H. Stockmayer: J. Chem. Phys. **36**, 227 (1962)
106. P.H. Verdier: J. Comput. Phys. **4**, 227 (1969)
107. For a review, see K. Binder. In: *Monte Carlo and Molecular Dynamics Simulations in Polymer Science*, ed by K. Binder (Oxford University Press, New York Oxford 1995) p 3
108. C.A. Vincent: Electrochimica Acta **40**, 2035 (1995)
109. M.G. McLin, C.A. Angell: Solid State Ionics **53**–**56**, 1072 (1992)
110. A. Voronel, E. Veliyulin, V.S. Machavariani, A. Kislink, D. Quitmann: Phys. Rev. Lett. **80**, 2630 (1998)
111. M. Duclot, F. Alloin, O. Brylev, J.Y. Sanchez, J.L. Souquet: Solid State Ionics **136**–**137**, 1153 (2000)
112. O. Dürr, W. Dieterich, A. Nitzan: J. Chem. Phys. **121**, 12732 (2004)
113. S.F. Druger, A. Nitzan, M.A. Ratner: J. Chem. Phys. **79**, 3133 (1983)
114. S.F. Druger, M.A. Ratner, A. Nitzan: Phys. Rev. B **31**, 3939 (1985)
115. A.K. Harrison, R. Zwanzig: Phys. Rev. A **32**, 1072 (1985)

116. R. Hilfer, R. Orbach. In: *Dynamical Processes in Condensed Molecular Systems*, ed by J. Klafter, J. Jortner, A. Blumen (World Scientific, Singapore 1989) p 175
117. S.F. Druger, M.A. Ratner: Phys. Rev. B **38**, 12589 (1988)
118. O. Dürr, W. Dieterich, A. Nitzan. In: *Multiscale Computational Methods in Chemistry and Physics*, NATO Science Series III, vol 177, ed by A. Brandt, J. Bernholc, K. Binder (IOS Press, Amsterdam 2001) p 288
119. R. Granek, A. Nitzan: J. Chem. Phys. **92**, 1329 (1990); **93**, 5918 (1990); M. Silverberg, M.A. Ratner, R. Granek, A. Nitzan: J. Chem. Phys. **93**, 3420 (1990)
120. K.S. Mendelson, M.H. Cohen: Geophysics **47**,257 (1982)
121. P. Maass, M. Meyer: J. Chem. Phys. **103**, 5776 (1995)